

Tetracycline sorption by magnetic biochar derived from
watermelon rind: performance and influential factors



A Thesis Submitted in Partial Fulfillment of the Requirements
for the Degree of Master of Engineering in Chemical Engineering
Department of Chemical Engineering
FACULTY OF ENGINEERING
Chulalongkorn University
Academic Year 2021
Copyright of Chulalongkorn University

การดูดซับเตตราไซคลินด้วยไบโอซามาแม่เหล็กที่สังเคราะห์จากเปลือกแตงโม: สมรรถนะ และ
ปัจจัยที่มีอิทธิพล



วิทยานิพนธ์นี้เป็นส่วนหนึ่งของการศึกษาตามหลักสูตรปริญญาวิทยาศาสตรมหาบัณฑิต
สาขาวิชาวิศวกรรมเคมี ภาควิชาวิศวกรรมเคมี
คณะวิศวกรรมศาสตร์ จุฬาลงกรณ์มหาวิทยาลัย
ปีการศึกษา 2564
ลิขสิทธิ์ของจุฬาลงกรณ์มหาวิทยาลัย

Thesis Title Tetracycline sorption by magnetic biochar derived from
watermelon rind: performance and influential factors
By Mr. Phisit Thairattananon
Field of Study Chemical Engineering
Thesis Advisor Professor TAWATCHAI CHARINPANITKUL

Accepted by the FACULTY OF ENGINEERING, Chulalongkorn University
in Partial Fulfillment of the Requirement for the Master of Engineering

----- Dean of the FACULTY OF
ENGINEERING
()

THESIS COMMITTEE

----- Chairman
(Assistant Professor SUPHOT PHATANASRI)
----- Thesis Advisor
(Professor TAWATCHAI CHARINPANITKUL)
----- Examiner
(Assistant Professor Rungthiwa Methaapanon)
----- External Examiner
(Assistant Professor Dr. Sakhon Ratchahat)


จุฬาลงกรณ์มหาวิทยาลัย
CHULALONGKORN UNIVERSITY

พิธีญัฐ ไทยรัตนานนท์ : การดูดซับเตตราไซคลินด้วยไบโอชาแม่เหล็กที่สังเคราะห์จากเปลือกแตงโม: สมรรถนะ และปัจจัยที่มีอิทธิพล. (Tetracycline sorption by magnetic biochar derived from watermelon rind: performance and influential factors) อ.ที่ปรึกษาหลัก : ศ. ดร.ธวัชชัย ชรินพานิษฐกุล

ยาปฏิชีวนะเตตราไซคลินเป็นหนึ่งในสารปนเปื้อนที่เกิดขึ้นใหม่ในแหล่งน้ำซึ่งก่อให้เกิดผลกระทบต่อสิ่งแวดล้อมและสุขภาพของมนุษย์ ไบโอชาแม่เหล็กถือเป็นตัวดูดซับที่มีแนวโน้มดีในกระบวนการดูดซับสำหรับการกำจัดสิ่งปนเปื้อนด้วยการทำงานที่มีประสิทธิภาพสูงและสะดวก ในงานนี้ไบโอชาแม่เหล็กถูกสังเคราะห์โดยนำเปลือกแตงโมที่หุบด้วยเหล็ก (III) คลอไรด์มาไพโรไลซิสที่อุณหภูมิไพโรไลซิสที่แตกต่างกันในช่วง 600-900 องศาเซลเซียส ก่อนใช้สำหรับการดูดซับเตตราไซคลิน วิเคราะห์ลักษณะของไบโอชาแม่เหล็ก โดยกล้องจุลทรรศน์อิเล็กตรอนแบบส่องกราด เครื่องวิเคราะห์องค์ประกอบ การดูดซับ/คลายตัวของไนโตรเจน ฟลูออรีนทรานส์ฟอร์มันอินฟราเรดสเปกโทรสโกปี รามานสเปกโทรสโกปี เครื่องวัดคุณสมบัติของแม่เหล็กของวัสดุแบบสั้น และเทคนิคการเลี้ยวเบนของรังสีเอกซ์ ได้มีการศึกษาจลนพลศาสตร์การดูดซับ ไอโซเทอม ผลกระทบของ pH ของสารละลาย และความสามารถในการนำกลับมาใช้ใหม่ นอกจากนี้ยังมีการศึกษาการสร้างแบบจำลองของสมรรถนะการดูดซับเตตราไซคลินภายใต้ปัจจัยที่มีอิทธิพลต่างๆ โดยใช้ response surface methodology (RSM) และ machine learning (ML) จากผลการทดลองพบว่า การเพิ่มขึ้นของอุณหภูมิไพโรไลซิสจาก 600 เป็น 900 องศาเซลเซียส ส่งผลอย่างมีนัยสำคัญต่อคุณลักษณะของไบโอชาแม่เหล็ก จลนพลศาสตร์การดูดซับของไบโอชาแม่เหล็กที่สังเคราะห์ที่อุณหภูมิ 600 องศาเซลเซียสเป็นไปตามแบบจำลองจลนพลศาสตร์อันดับหนึ่งในขณะที่ของไบโอชาแม่เหล็กที่สังเคราะห์ที่อุณหภูมิ 700 800 และ 900 องศาเซลเซียสเป็นไปตามแบบจำลองจลนพลศาสตร์อันดับสอง ไอโซเทอมการดูดซับเข้ากันได้ดีกับไอโซเทอมของฟรุนดลิช ซึ่งยืนยันว่าเป็นการดูดซับที่ตำแหน่งแตกต่างกัน นอกจากนี้ ไบโอชาที่สังเคราะห์ที่อุณหภูมิ 900 องศาเซลเซียสมีสมรรถนะในการดูดซับสูงสุดสูงสุดที่ 77.60 มก./กรัม กระบวนการดูดซับขึ้นอยู่กับค่า pH การทดสอบความสามารถในการนำกลับมาใช้ใหม่เผยให้เห็นความสามารถในการดูดซับลดลงจาก 100 เป็น 83.89 เปอร์เซ็นต์หลังจากใช้งานไปห้ารอบ ผล ANOVA ยังยืนยันว่าแบบจำลองมีนัยสำคัญที่ความเชื่อมั่น 95% นอกจากนี้ ลำดับของปัจจัยที่มีอิทธิพลคือ pH ของสารละลาย > ปฏิสัมพันธ์ระหว่างความเข้มข้นของเริ่มต้นของเตตราไซคลิน และ pH ของสารละลาย > ผลกำลังสองของความเข้มข้นเริ่มต้นของเตตราไซคลิน > ความเข้มข้นเริ่มต้นของเตตราไซคลิน การพัฒนาแบบจำลองโดยใช้อัลกอริทึมของ ML ที่แตกต่างกันสามชนิด พบว่า Catboost มีประสิทธิภาพเหนือกว่า random forest และ boosted regression tree ความสำคัญของลักษณะเผยให้เห็นว่าพื้นที่ผิวจำเพาะมีอิทธิพลต่อสมรรถนะการดูดซับเตตราไซคลินมากที่สุดตามมาด้วย (O+N)/C ความเข้มข้นเริ่มต้นของเตตราไซคลิน H/C และ C% ตามลำดับ

สาขาวิชา วิศวกรรมเคมี
ปีการศึกษา 2564

ลายมือชื่อนิสิต
ลายมือชื่อ อ.ที่ปรึกษาหลัก

6370204721 : MAJOR CHEMICAL ENGINEERING

KEYWORD Tetracycline, Adsorption, Magnetic biochar

D:

Phisit Thairattananon : Tetracycline sorption by magnetic biochar derived from watermelon rind: performance and influential factors. Advisor: Prof. TAWATCHAI CHARINPANITKUL

Tetracycline (TC) antibiotic is one of emerging contaminants in water reservoirs that causes undesirable effects on environment and human health. Magnetic biochar (MBC) is considered a promising sorbent in adsorption process for removal of contaminants with highly efficient and facile operation. In this work, MBC was synthesized by pyrolysis of watermelon rind impregnated with FeCl_3 at different pyrolysis temperatures in a range of 600-900 °C prior to applying for TC adsorption. Characteristics of MBC were analyzed by scanning electron microscopy, elemental analyzer, N_2 adsorption/desorption, Fourier-transform infrared spectroscopy, Raman spectroscopy, vibrating sample magnetometry, and X-ray diffractometry. The adsorption kinetics, isotherm, effect of solution pH, and reusability were investigated. Moreover, an empirical and semi-empirical model of TC adsorption capacity under influential factors based on response surface methodology (RSM) and machine learning (ML) were developed. From the results, an increase in the pyrolysis temperature from 600 to 900 °C significantly affects on characteristics of MBC. The adsorption kinetics of MBC600 follows pseudo-first-order kinetic model while MBC700, MBC800, and MBC900 follow pseudo-second-order kinetic model. The adsorption isotherm fitted well with Freundlich isotherm investigating heterogeneous adsorption site. In addition, the highest maximum adsorption capacity of 77.60 mg/g could be obtained from MBC900. The adsorption process is pH-dependent. The reusability test revealed adsorption capacity decrease from 100 to 83.89% after five cycles. ANOVA results confirmed an empirical model was significantly at 95% confidence. In addition, the order of influential terms is solution pH > interaction between initial TC concentration and solution pH > square effect of initial TC concentration > initial TC concentration. Three different ML algorithms were used to develop the semi-empirical model. It was found that Catboost outperformed random forest and boosted regression tree. The feature important revealed S_{BET} provided the largest effect on TC adsorption capacity followed by (O+N)/C, initial TC concentration, H/C, and C%, respectively.

Field of Study: Chemical Engineering

Student's Signature

.....

Academic 2021

Advisor's Signature

.....

Year:

ACKNOWLEDGEMENTS

I would first like to sincerely thanks to my advisor, Prof. Tawatchai Charinpanitkul from Department of Chemical Engineering, Chulalongkorn University for his continuous support, feedback, encouragement, valuable guidance to complete my thesis.

I would like to acknowledge Dr. Giang T. T. Le for her help throughout my thesis. Additionally, I am also thankful to all members of Prof. Tawatchai's research group for the collaboration. especially, Mr. Tanapat Rodruangnon for suggestions and his help with the experimentation.

Furthermore, I would like to thank the funding support from Ratchadapisek Somphot Fund, Chulalongkorn University for CEPT and NANOTEC, NSTDA, Ministry of Higher Education, Science, Research and Innovation, Thailand through the program of Research Network of NANOTEC (RNN).

Finally, I would like to thank to my parents for their support throughout this research.

จุฬาลงกรณ์มหาวิทยาลัย
CHULALONGKORN UNIVERSITY

Phisit Thairattananon

TABLE OF CONTENTS

	Page
.....	iii
ABSTRACT (THAI)	iii
.....	iv
ABSTRACT (ENGLISH)	iv
ACKNOWLEDGEMENTS	v
TABLE OF CONTENTS	vi
LIST OF TABLES	viii
LIST OF FIGURES	ix
CHAPTER 1 INTRODUCTION	1
1.1 Motivation for this research work.....	1
1.2 Research objectives	3
1.3 Scope of this research	3
1.4 Expected benefit	4
CHAPTER 2 FUNDAMENTAL KNOWLEDGE	5
2.1 Contamination of tetracycline in water reservoirs.....	5
2.2 Treatment method.....	6
2.3 Biochar-based sorbents	7
2.4 Synthesis of MBC.....	8
2.5 Response surface methodology	9
2.6 Machine learning	10
2.7 Literature review.....	12
CHAPTER 3 METHODOLOGY	22
3.1 Chemicals and materials	22
3.2 Synthesis of MBC.....	23
3.3 Characterization techniques.....	24

3.4 Adsorption experiments	29
3.5 Development of model	30
CHAPTER 4 RESULTS AND DISCUSSION.....	33
4.1 Effects of pyrolysis temperature on characteristics of pyrolyzed products	33
4.2 Adsorption experiments	43
4.3 Development of an empirical model of TC adsorption capacity	51
CHAPTER 5 CONCLUSIONS AND RECOMMENDATIONS	61
5.1 Conclusions.....	61
5.2 Recommendations for future work	64
APPENDIX A Preparation of watermelon rind impregnated with FeCl ₃	65
APPENDIX B Size analysis of magnetic particle	66
APPENDIX C Product yield of synthesized MBC.....	69
APPENDIX D Curve fitting of Raman spectra	71
APPENDIX E Adsorption of TC.....	73
APPENDIX F Source code of ML.....	77
REFERENCES	88
VITA.....	95

LIST OF TABLES

Table 2.1 Yield of MBC [55]	14
Table 2.2 The studied factors and levels [57]	20
Table 2.3 The studied factors and levels [58]	20
Table 2.4 The studied factors and levels [59]	21
Table 3. 1 The elemental content of watermelon rind.....	23
Table 3.2 The studied factors and levels used to design experimental runs	30
Table 3.3 Experimental runs designed based on CCD.....	31
Table 4.1 S_{BET} , V_p , and yield of different MBC samples.....	35
Table 4.2 Chemical composition of MBCs	37
Table 4.3 Saturation magnetization (M_s) and Coercivity (H_c) of pyrolyzed samples	43
Table 4.4 Adsorption kinetics parameter	46
Table 4.5 Adsorption isotherm parameter.....	49
Table 4.6 Experimental and predicted adsorption capacity under CCD design.....	52
Table 4.7 ANOVA of prediction model of tetracycline adsorption capacity.....	54
Table B.1 Diameter analysis data of α -Fe.....	67
Table C.1 Weight of watermelon rind impregnated with $FeCl_3$ and weight of product at various pyrolysis temperatures.....	69
Table C.2 Product yield (%) of synthesized MBC at various pyrolysis temperatures	70
Table E.1 Experimental data of TC adsorption capacity of MBCs at different contact times.....	73
Table E. 2 Experimental data of TC adsorption isotherm with initial TC concentration varied from 10-100 mg/L.....	75

LIST OF FIGURES

Fig. 2.1 (a) SEM and (b) TEM image of MWBC sample [54].....	13
Fig. 2.2 FTIR spectrum of MBC and MWBC [54]	13
Fig. 2.3 FESEM images of (a) MBC600, (b) MBC700, and (c) MBC900 [55].....	15
Fig. 2.4 SEM image of (a) MBC500, (b) MBC600, (c) MBC700, (d) MBC800 [56] 16	16
Fig. 2.5 Raman spectra of MBC samples [56].....	17
Fig. 2.6 XRD pattern of MBC [55].....	18
Fig. 2.7 XRD pattern of MBC [56].....	19
Fig. 3.1 Morphology of watermelon rind.....	22
Fig. 3.2 The experimental schematic of MBC synthesis	23
Fig. 3.3 Environmental scanning electron microscope model Quanta450	24
Fig. 3.4 Element analyzer model Thermo flash 2000.....	25
Fig. 3.5 Surface area and porosimetry analyzer model ASAP2460	26
Fig. 3.6 FTIR spectrometer model Nicolet 6700.....	26
Fig. 3.7 Raman spectroscopy model NTEGRA spectra	27
Fig. 3.8 Vibrating sample magnetometer model 7404	28
Fig. 3.9 X-ray diffraction spectroscopy model D8 Discover.....	28
Fig. 4.1 SEM images of pyrolyzed samples obtained at pyrolysis temperature of (a) 600 (b) 700 (c) 800 (d) 900 °C.....	34
Fig. 4.2 Pore size distribution of pyrolyzed samples.....	36
Fig. 4.3 FTIR spectra of different MBC samples	38
Fig. 4.4 Raman spectra of pyrolyzed samples	39
Fig. 4.5 Magnetic phases of pyrolyzed samples	40
Fig. 4.6 Magnetic hysteresis of pyrolyzed samples.....	42
Fig. 4.7 Dispersion of MBC900 (a) before induced by external magnet (b) induced by external magnet (c) after removing external magnet	42
Fig. 4.8 (a) Adsorption kinetics, (b) Linearized pseudo-first-order kinetic model, and (c) Linearized pseudo-second-order kinetic model.....	45

Fig. 4.9 (a) Adsorption isotherm, (b) Linearized Langmuir isotherm model, and (c) Linearized Freundlich isotherm model	48
Fig. 4.10 Effect of initial pH on TC adsorption capacity	50
Fig. 4.11 Reusability of MBC900.....	51
Fig. 4.12 Predicted adsorption capacity against experimental data (red line is regression line and blue line is perfect line ($y=x$))	53
Fig. 4.13 Sum of squares of significantly terms	55
Fig. 4.14 3-D surface plots of an interaction effect between (a) Initial TC concentration and contact time (b) Solution pH and adsorbent dosage (c) Initial TC concentration and solution pH on adsorption capacity	57
Fig. B1 SEM image of MBC900 (red line shows how to collect the data for imageJ).....	66



CHAPTER 1

INTRODUCTION

1.1 Motivation for this research work

Tetracycline (TC) is one of widely used antibiotics for suppression of bacteria and pathogens in humans and animals and is used as growth stimulant in animal husbandry and aquaculture [1] because TC provides good antimicrobial properties and absence of adverse side effects [2]. However, 30-90% of TC cannot be metabolized [3] along with the use of antibiotics in aquaculture, crop growing, and contaminated sewage sludge from antibiotic manufacturing, leading to excessive release of TC to water reservoirs [4]. It causes undesirable effects with antibiotic resistance genes(ARG) and antibiotic-resistant bacteria(ARB) [5], which could contaminate in human food chain. When humans consume those contaminated, it will lead to increased medical costs and rate of mortality [6]. Therefore, antibiotics have become an emerging contaminant. Among various methods for the removal of antibiotics from contaminated water, including biological treatment, advanced oxidation process, and membrane filtration, adsorption is a common method due to its advantages of low cost, high removal efficiency, and easy operation [7].

In comparison to carbon nanotubes and activated carbon, biochar is recognized as a cost-effective and renewable sorbent [4], which can be produced from agricultural wastes. Global total watermelon production in 2020 was 101.62 million tons, which covered 11.46% of overall fruit production [8]. Approximately 30% of the total mass of watermelon is its rind [9], resulting in a large amount of agricultural waste. Watermelon rind is composed of carbon-rich material, such as cellulose, and pectin [10]. Moreover, it contains alkaline, alkaline earth, and other metals [11, 12], which can activate and create porosity of biochar during pyrolysis [13]. Therefore, watermelon rind is a promising raw material to produce biochar and the utilization of watermelon rind could reduce agricultural waste. However, pristine biochar possesses low specific surface area resulting in poor TC adsorption capacity[14]. Chemical modification of biochar could improve desirable characteristics of biochar along with

enhancing adsorption capacity [15], especially modified by an iron compound known as magnetic biochar(MBC), which not only enhances adsorption capacity but also ease the separation and recycling of spent sorbent [16] via utilizing its magnetic property. MBC can be synthesized from various methods, such as impregnation-pyrolysis [17], chemical co-precipitation [18], solvothermal [19], and reductive co-precipitation [20]. Impregnation-pyrolysis can provide MBC with one-step synthesis including both magnetization and pyrolysis of biochar [21]. Biochar synthesized from watermelon rind has been applied for adsorption of heavy metals and dyes [22]. However, synthesized MBC from watermelon rind as sorbent for TC adsorption is still limited. There are two key factors could significantly affect TC adsorption capacity, including physicochemical properties of adsorbent (which depends on pyrolysis conditions) and adsorption conditions (initial TC concentration, adsorbent dosage, solution pH, and contact time).

However, batch adsorption experiments are often high cost and time-consuming. Accordingly, it would be useful to develop empirical models for TC adsorption capacity [23]. Central composite design (CCD) is a useful approach in response surface methodology (RSM) for designing a small number of experimental runs compared with “one variable at a time” approach [24]. RSM possesses the ability to evaluate the combined effect of all factors, modeling, and optimization [25]. Machine learning (ML) algorithms such as random forest, Catboost, and boosted regression tree could deal with complex and non-linear problem [26].

This research aims to synthesize MBC by pyrolysis of watermelon rind-impregnated with FeCl_3 for TC adsorption. The effect of pyrolysis temperature on characteristics of MBCs was investigated. TC adsorption kinetics and isotherm of MBCs were investigated. CCD was applied to design experimental runs, then RSM and was applied to develop the empirical models of TC adsorption capacity under various influential factors i.e., initial TC concentration, adsorbent dosage, solution pH, and contact time. ML algorithms such as random forest, Catboost, and boosted regression tree were applied to develop the semi-empirical model of TC adsorption capacity under collected data of S_{BET} , H/C, (O+N)/C, C%, and initial TC concentration.

MBC was characterized by using an environmental scanning electron microscope (ESEM), Element analyzer, N₂ adsorption/desorption, Fourier-transform infrared spectroscopy (FTIR), Raman spectroscopy, vibrating sample magnetometer (VSM), and X-ray diffraction spectroscopy (XRD).

1.2 Research objectives

This research aims to synthesize MBC from watermelon rind for TC adsorption. Effect of pyrolysis temperature on characteristics of MBCs was investigated. The adsorption experiments were investigated. An empirical and semi-empirical model of TC adsorption capacity were developed using RSM and ML under influential factors.

1.3 Scope of this research

The scope of this research consists of 3 parts, which are synthesized MBC by pyrolysis of watermelon rind-impregnated with FeCl₃, TC adsorption experiments, and generation of a prediction model

1.3.1 Synthesis of MBC by pyrolysis of watermelon rind-impregnated with FeCl₃

MBCs were synthesized from pyrolysis of watermelon rind impregnated with FeCl₃ when impregnation ratio of FeCl₃ to watermelon rind is 2:1 at various temperatures (600, 700, 800, and 900°C) under N₂ atmospheric. The characterization of MBC using SEM, Element analyzer, N₂ adsorption/desorption isotherms, FTIR, Raman spectroscopy, VSM, and XRD.

1.3.2 TC adsorption experiments

MBCs were employed as sorbents for adsorption of TC for investigating the adsorption kinetic, isotherm, effect of initial pH, and reusability of MBCs. The concentration of TC was measured by UV-VIS.

1.3.3 Development of an empirical model

MBC pyrolyzed from designed pyrolysis temperature was used for another adsorption experiment designed by CCD. Then RSM was applied to develop the empirical model of TC adsorption capacity. ML algorithms were

used to develop semi-empirical models of TC adsorption capacity from collected data.

1.4 Expected benefit

Understanding of MBC synthesis by pyrolysis of watermelon rind-impregnated with FeCl_3 at different pyrolysis temperatures would be obtained. Ability in TC adsorption and development of empirical model would be obtained. Moreover, the ability to interpret the characterization results and explain the effect of influential factors would be investigated.



CHAPTER 2 FUNDAMENTAL KNOWLEDGE

2.1 Contamination of tetracycline in water reservoirs

Approximately 70% of global antibiotic is used whether for suppression of bacteria and growth stimulant in animals or crop growing. Another 30% is used for suppression of bacteria in humans [27]. Van Boeckel et al. [28] used statistical models combine with livestock densities, demand for meat products, and antibiotic consumption to estimate the global consumption of antibiotics in animals that will increase from 63,000 tons to 105,600 tons from 2010 to 2030 due to the rising of animal protein demand for humans. Eili Klein et al. [29] used a database of antibiotic sales in 76 countries from 2000 through 2015 to estimate global antibiotic consumption that increased by 65% from 21.1 to 34.8 billion defined daily doses and to project that will increase by 200% from 2015 to 2030. Therefore, the excessive consumption of antibiotics has become a serious problem.

Tetracycline is one of the most used antibiotics due to its good antimicrobial properties and absence of side effects [2]. The widely and excessive use of tetracycline causes releasing of tetracycline into the water reservoirs by several pathways including manufacturing pharmaceuticals; wastewater from treatment plants can detect a significantly residual antibiotic [30], human consumption; unmetabolized antibiotics further transported from sewage sludge to soil and water reservoirs[4], animal consumption; unmetabolized antibiotics is a contaminant in manures can further enter water reservoirs [31], the use of antibiotics in aquaculture, it can directly enter water reservoirs [27], and crop growing; during spraying, antibiotics can enter soil and water reservoirs. Tetracycline is the most frequently detected antibiotic in manures [32] and seawater [33]. The contamination of tetracycline in water can further contaminate food products and drinking water [30]. Consumption of contaminated food and water causes antibiotic resistance leading to higher medical costs and an increased rate of mortality [6].

2.2 Treatment method

There are various methods for removal of antibiotics such as biodegradation [34], advanced oxidation process [35], membrane filtration [36], and adsorption [7].

2.2.1 Biodegradation

Biodegradation is one of important methods for antibiotic degradation in wastewater. Generally, biodegradation is combined with adsorption in biological wastewater treatment. Biodegradation rate in TC is quite slow. However, it is important for sulfamethazine and trimethoprim. The major benefit of this method is can transmit antibiotics into small molecules i.e., H₂O and CO₂, which does not cause environmental risk [34].

2.2.2 Advanced oxidation process

Hydroxyl radical is the main character of advanced oxidation process. With the high reactive hydroxyl radical, it would react with antibiotic molecules very fast. Hydroxyl radicals could degrade antibiotic molecules by attacking antibiotic molecules at high electron density sites and generating a chain of oxidation reactions. However, this process requires chemicals for generating the hydroxyl radical such as ozone and hydrogen peroxide [35].

2.2.3 Membrane filtration

Membrane filtration is a process with pressured driving force. This process provides both mechanical and chemical sieving of contaminated molecules with high efficiency. However, fouling could occur on membrane surface so regeneration of the membrane is needed [37].

2.2.4 Adsorption

Adsorption is a transfer process between liquid bulk called adsorbate and solid called adsorbent. The adsorption process could occur in both physical and chemical adsorption [38]. Various types of adsorbents are available such as activated carbon and biochar which can be produced from agricultural waste. The operation of this process is simple with high efficiency could be obtained [7].

Among various methods for removal of antibiotics, adsorption is recognized as low cost, high removal efficiency, and easy operation. Therefore, it is employed in this work.

2.3 Biochar-based sorbents

Based on synthesis method, biochar-based sorbents could be divided into pristine biochar and modification biochar.

2.3.1 Pristine biochar

Pristine biochar is a carbon-rich solid product obtained from pyrolysis of biomass under oxygen-limited [39-41]. Slow pyrolysis with heating rate (<10 °C/min) provides favored yield of resultant biochar [42]. Biochar has been used as sorbents for adsorption of contaminants in soil and water[41], due to favorable physicochemical surface characteristics [43]. However, pristine biochar exhibited unsatisfactory adsorption capacity in the case of adsorption mechanism based on pore filling, due to low specific surface area and pore volume [4, 14].

2.3.2 Modification biochar

Modification of biochar including physical and chemical modification could develop pore structure and improve surface functional groups of biochar.

Physical modification

Steam/gas activation, ball milling, and microwave are physical modification methods, which could improve pore structure and lead to enhanced adsorption capacity without adding any impurities [44].

Chemical modification

Modification by oxidizing agents including H_3PO_4 , H_2SO_4 , HNO_3 , HCl , H_2O_2 , and $KMnO_4$ could oxidize surface of biochar to hydroxyl and aldehyde groups leading to ability in binding cation along with development of microporous and S_{BET} [44-46].

Modification by reducing agents including NaOH, KOH, and NH₄OH could decrease hydroxyl functional groups on biochar surface increasing hydrophobicity as well as significantly increasing porosity [45].

Modification methods including physical modification, modification by oxidizing agents, and reducing agents could develop porosity of biochar and enhance adsorption capacity. However, it is hard to separate and recycle spent sorbent. Modification by iron compound known as magnetic biochar (MBC) could solve the above problem via utilizing its magnetic property. It also improves porosity of biochar leading to enhance adsorption capacity [21].

2.4 Synthesis of MBC

Commonly, there are four synthesis routes to produce MBC, such as Impregnation-pyrolysis, chemical co-precipitation, solvothermal, and reductive co-precipitation [21].

2.4.1 Impregnation-pyrolysis

Pyrolysis is thermal decomposition of biomass in absence of oxygen[47], which is divided into conventional pyrolysis, fast pyrolysis, and flash pyrolysis. Generally, conventional pyrolysis is used for production of MBC, because the highest biochar yield could be obtained. First, biomass was impregnated with magnetic precursor solution. Then, placed in furnace for pyrolysis. In this process, biomass can be activated to biochar and magnetic precursor can be transformed into magnetic particle [21]. MBC produced from this method provides good stability and less metal leaching during preparation. However, tar and gas pollutants were produced during pyrolysis[48, 49].

2.4.2 Chemical co-precipitation

First, biochar is immersed in magnetic precursor solution. Magnetic precursor commonly used is ferric and ferrous salts, the molar ratio of Fe³⁺ to Fe²⁺ is 2:1 [50]. Then, dropping alkaline solution, magnetic particles precipitate on biochar surface [21]. The Fe₃O₄ is completely precipitation at pH around 8-12 [51]. This process is easy to control, and MBC produced from this method provides excellent stability.

However, adding alkaline solution could increase cost, and wastewater of alkaline needs to be treated [21].

2.4.3 Solvothermal

Solvothermal is thermal treatment method for removing water, CO₂, SO₄, and other volatile components. Generally, solvothermal is used for production of magnetic nanomaterials. MBC produced from this process is biomass and magnetic precursor placed in pressurized autoclave with operating temperature of 100-300 °C. Reductants, alkaline salts, and surfactants are needed to add in solvothermal method for preventing agglomeration of particles [21].

2.4.4 Reductive co-precipitation

Reductive co-precipitation is adding reductants such as NaBH₄ to mixed solution of Fe²⁺/Fe³⁺ and biochar. The reductants can reduce Fe²⁺/Fe³⁺ to zero-valent iron [21].

Among various methods for synthesis of MBC, impregnation-pyrolysis has several advantages, such as time-saving, due to pyrolysis and magnetization of biochar are completed at the same time. Therefore, it is employed in this work.

2.5 Response surface methodology

Adsorption model could help to save time and cost, response surface methodology is one of powerful tools for modeling.

Response surface methodology (RSM) is a group of mathematical and statistical techniques used to define relationships between response and input variables (or independent variables) [52]. RSM is widely used for optimization and modeling, it has several advantages, such as it provides a lot of information with a small number of experiments, time-saving compared with one variable at a time technique, and ability in observed interaction effect of input variable [53].

The commonly used model in RSM is second-order model [54], which can be written as follow:

$$y = \beta_0 + \sum_{i=1}^k \beta_i x_i + \sum_{i=1}^k \beta_{ii} x_i^2 + \sum \sum_{i < j} \beta_{ij} x_i x_j + \varepsilon \quad (1)$$

where,

y is a response.

$\beta_0, \beta_i, \beta_{ii}, \beta_{ij}$ are regression coefficients of intercept, linear, quadratic, and interaction respectively.

x_i and x_j are input variables.

ε is a random experimental error.

2.6 Machine learning

Machine learning (ML) is a branch of artificial intelligence that can learn and make decisions from the data without program [55]. Generally, there are three types of ML such as supervised, unsupervised, and reinforcement learning. Supervised learning algorithms can be used to model relationships between independent variables and dependent variables known as labeled data. To build prediction model, first, labeled data is randomly separated into training data and testing data. Training data is used to build a statistical model via machine learning algorithms. Then, the statistical model is validated by testing data. Finally, prediction model is obtained [56]. Many ML algorithms could deal with complex relationships between independent variables and dependent variables[26], e.g. random forest, Catboost, and boosted regression tree.

2.6.1 Random forest

Random forest (RF) is a classification algorithm, which can used for regression problems. It is consist of many decision trees generated by bagging and random selection[57]. Schematic diagram of random forest is exhibited in **Fig. 2.1**. The advantages of this algorithm are high accuracy and resistant to overfitting[26].

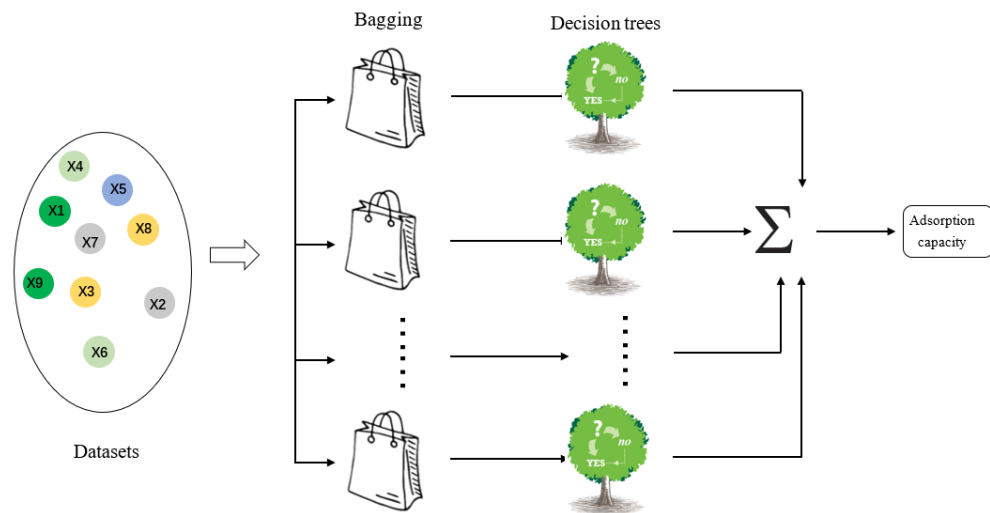


Fig. 2.1 Schematic diagram of random forest [23]

2.6.2 CatBoost

CatBoost or Categorical Boosting is one of ML algorithms, which generated by modification of gradient boosting algorithm with a new categorical features. In comparison to other boosting algorithms, CatBoost is outperformance in quality of variety of datasets. Moreover, it could deal with prediction shift of the present gradient boosting algorithms[58].

2.6.3 Boosted regression tree

Boosted regression tree (BRT) is algorithm that fitting many single models and combine them for optimizing prediction model. Two algorithms are used in BRT such as decision tree and boosting. This algorithm can be used with a variety of response types. It can accommodate missing data. Moreover, data transformation and elimination are no need for BRT[59].

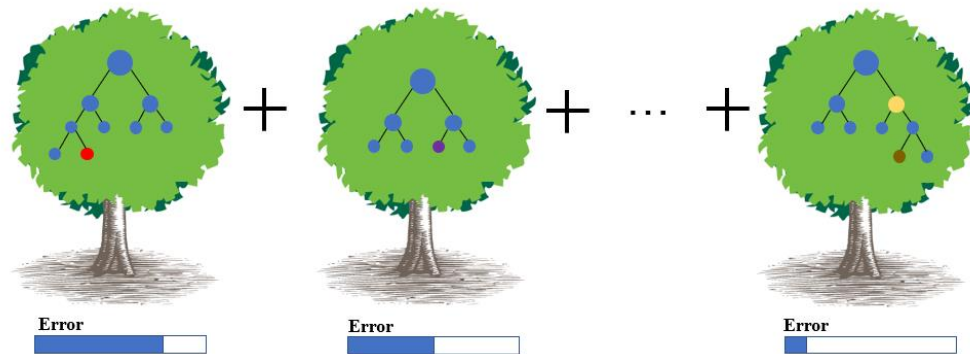


Fig. 2.2 Schematic diagram of boosted regression tree [23]

2.7 Literature review

Many years ago, many research about biochar and MBC synthesis have been developed to study the effect of various parameters on the characteristics of MBC. Among all parameters, the effect of pyrolysis temperature on characteristics of MBC and prediction model of TC adsorption capacity under various adsorption conditions have been reported in many research as follows.

2.5.1 Use of watermelon rind as a precursor for synthesis of magnetic biochar

Synthesis of magnetic watermelon rind biochar (MWBC) from watermelon rind was reported by Lingamdinne et al. [60]. They started by synthesis of biochar at various pyrolysis temperatures (300, 400, and 500 °C). They found that biochar pyrolyzed at temperature of 500 °C showed the highest removal of uranium. Therefore, they used biochar pyrolyzed from temperature of 500 °C for synthesis of WMBC. The MWBC was synthesized by chemical co-precipitation of $\text{FeCl}_3 \cdot 6\text{H}_2\text{O}$ and $\text{FeSO}_4 \cdot 7\text{H}_2\text{O}$ solution in molar ratio of 2:1. The process was adjusted pH to 10 by adding NH_3 solution for complete precipitation. Morphology of MWBC was observed by scanning electron microscope (SEM) as shown in **Fig. 2.1a**. Porous and rough surfaces of WMBC could be observed. Several black spots are present in TEM image as shown in **Fig. 2.1b** suggesting the co-precipitation method could provide uniform Fe_3O_4 particles on biochar.

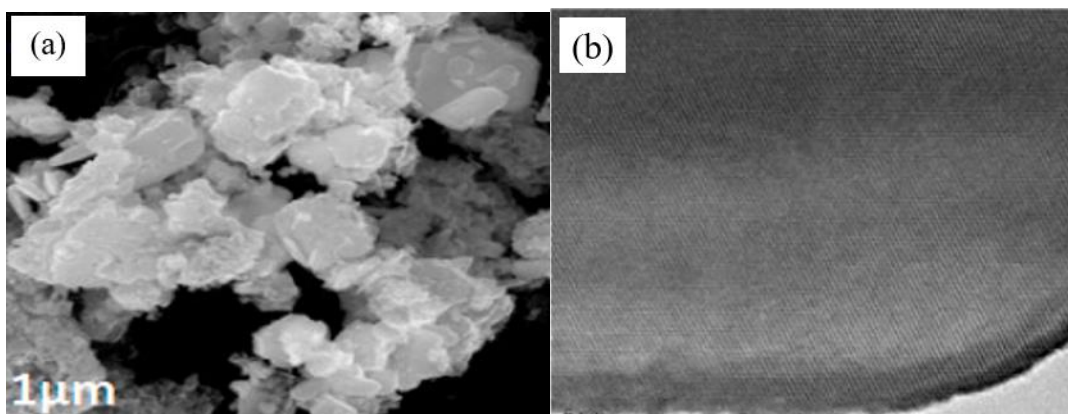


Fig. 2.3 (a) SEM and (b) TEM image of MWBC sample [60]

The characteristic bands of watermelon rind biochar (WBC) and MWBC are shown in **Fig. 2.2**. They found characteristic peaks of WBC around 3268, 1342, 1584 cm^{-1} , assigned to -OH, aliphatic C-H, and aromatic C=C respectively.

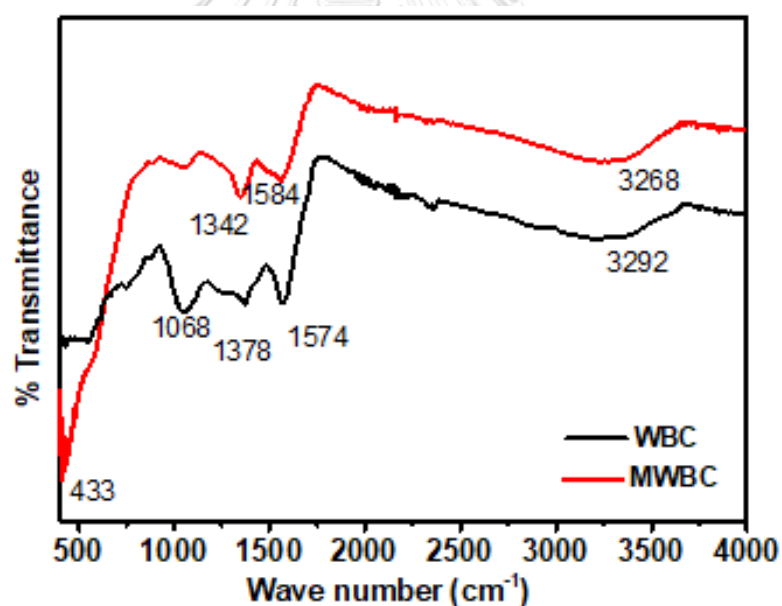


Fig. 2.4 FTIR spectrum of MBC and MWBC [60]

2.5.2 Effect of pyrolysis temperature on characteristics of magnetic biochar.

Pyrolysis temperature is a major factor that affects the characteristics of magnetic biochar. There were many studies reported on the effect of pyrolysis temperature on characteristics of magnetic biochar as follows.

Hu et al. [61] synthesized MBC by pyrolysis of rattan sawdust and iron salt. Rattan sawdust was used as a carbon precursor, then mixed with Fe^{2+} and Fe^{3+} solution. The mixture was pyrolyzed from room temperature to setting temperature (600, 700, 800, and 900 °C) with a heating rate of 5 °C/min. After holding for 2 hr in N_2 gas flow of 80 mL/min, MBC was obtained.

Jiang et al. [62] synthesized MBC by fast pyrolysis. Firstly, sawdust was immersed in $\text{FeCl}_3 \cdot 6\text{H}_2\text{O}$ solution, then shaken at 200 rpm for 5 hr. The rotary evaporation was used for removing water followed by drying at 80 °C overnight. The impregnated sawdust was pyrolyzed under N_2 gas flow of 400 mL/min. Pyrolysis temperatures varied from 500-800 °C while holding times also varied from 0-1 hr.

2.5.2.1 Yield of MBC product

From Hu et al. [61], they found that with an increase in pyrolysis temperatures from 600 °C to 900 °C increased degree of graphitization, resulting in yield of MBC decreasing from 34.49% to 25.30% as shown in **Table 2.1**.

Table 2.1 Yield of MBC [61]

Sample	Yield (%)
MBC600	34.49
MBC700	31.71
MBC800	24.82
MBC900	25.30

2.5.2.2 Morphology of MBC

From Hu et al. [61], they observed morphology of MBC by FESEM (FEIXL-30) and EDAX (FEG 132-10) with operating voltage of 20kV. It could be observed that iron particles formed on biochar surface. At pyrolysis temperatures of 600 °C and 700 °C, smooth and octahedral crystal faces of magnetic particles formed on

biochar matrix as exhibited in **Fig. 2.3a** and **Fig. 2.3b**. When pyrolysis temperatures increased to 900 °C, ovoid morphologies could be observed together with magnetic particles assembled as exhibited in **Fig. 2.3c**.

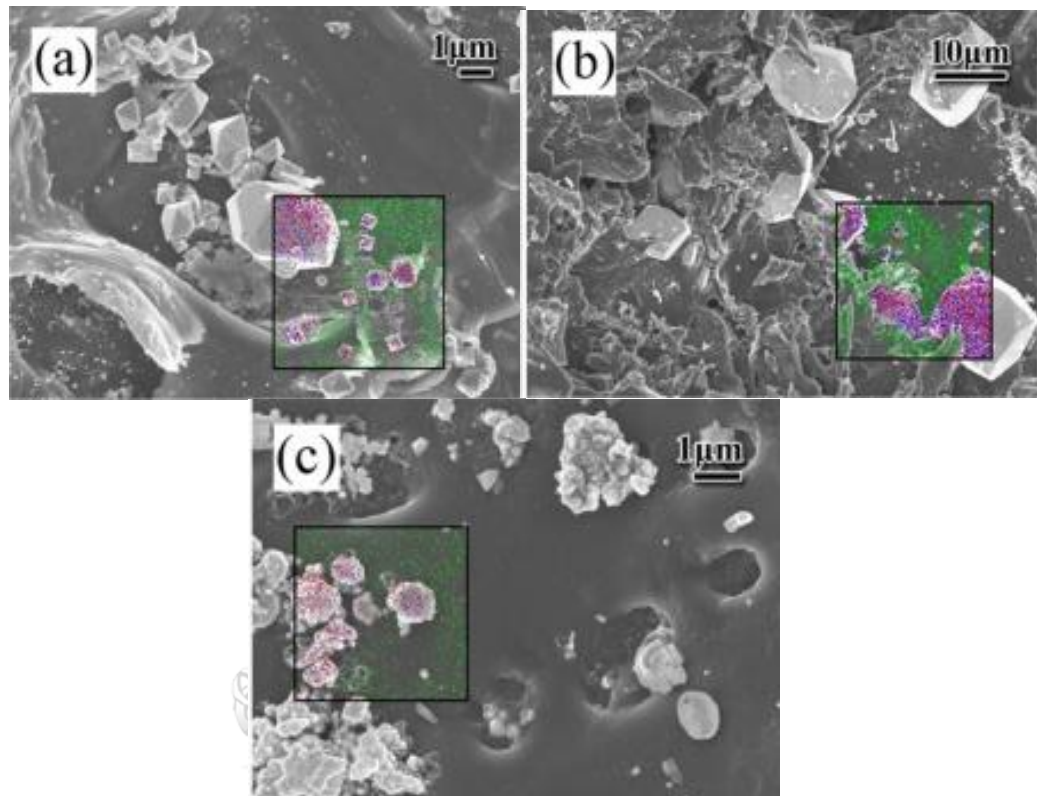


Fig. 2.5 FESEM images of (a) MBC600, (b) MBC700, and (c) MBC900 [61]

From Jiang et al. [62], they observed morphology of MBC by SEM (FEI Company, Hillsboro, OR, USA). A large nanoparticle could be observed in MBC500 as shown in **Fig. 2.4a**. Some small nanofibers were formed when pyrolysis temperature increased to 600 °C (**Fig. 2.4b**). With pyrolysis temperatures of 700 °C and 800 °C, more nanofibers formed together with more regular morphology.

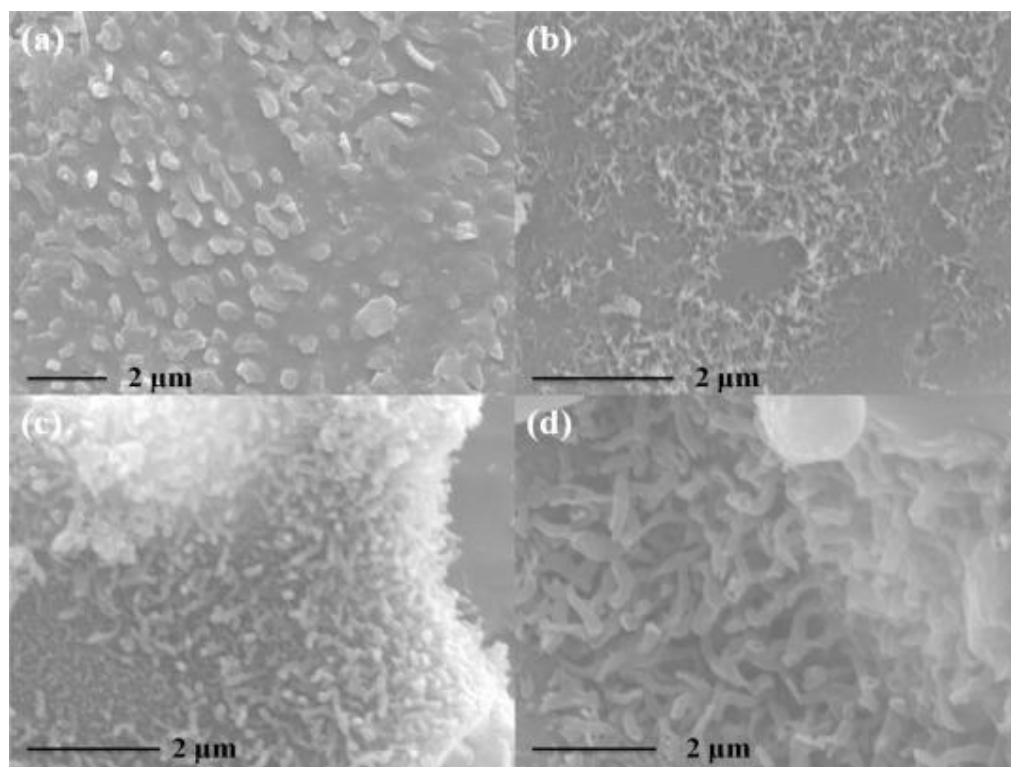


Fig. 2.6 SEM image of (a) MBC500, (b) MBC600, (c) MBC700, (d) MBC800 [62]

2.5.2.3 Crystallinity of MBC

Jiang et al. [62], used Raman spectroscopy (LabRamHR, HORIBA Jobin Yvon, Paris, France) to analyze the crystallinity of MBC. 1355 cm^{-1} according to D band which represented amorphous carbon. The peak at 1592 cm^{-1} according to G band represented graphitic carbon. With an increase in pyrolysis temperatures from $500\text{ }^{\circ}\text{C}$ to $800\text{ }^{\circ}\text{C}$, I_G/I_D ratio was increased from 1.06 to 1.27. The results indicate the degree of graphitization increase with pyrolysis temperatures.

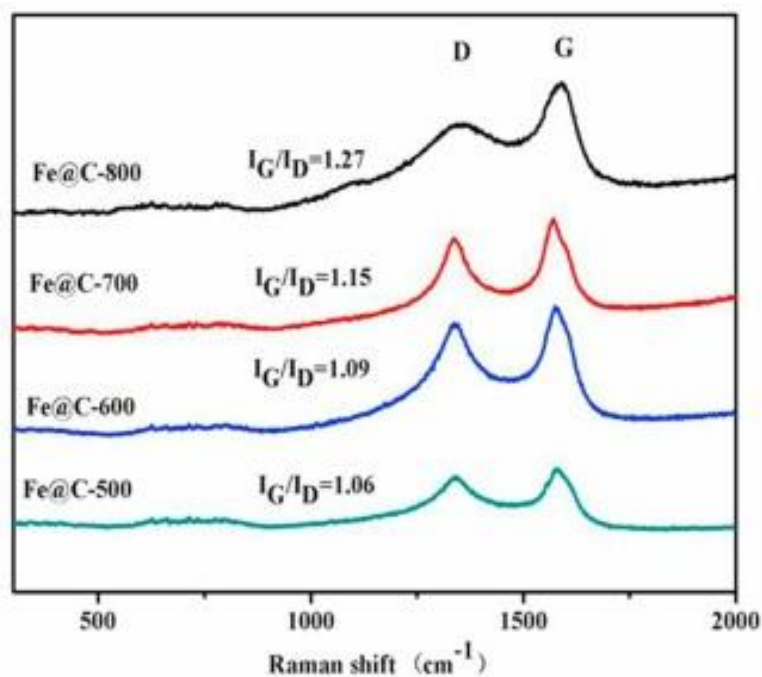


Fig. 2.7 Raman spectra of MBC samples [62]

2.5.2.4 Magnetic phase of MBC

From Hu et al. [61], they used an X-ray diffractometer with 40 keV, 40 mA, and $\lambda = 1.5460 \text{ \AA}$ to identify magnetic phase of MBC between 2θ of $10\text{--}80^\circ$. XRD patterns of MBC are exhibited in **Fig 2.6**. The peaks at $2\theta = 18.2^\circ, 30.0^\circ, 35.4^\circ, 43.0^\circ, 56.9^\circ,$ and 62.5° (JCPDS 89-0688) attributed to Fe_3O_4 were found in MBC600. When pyrolysis temperatures were increased to 700°C and 800°C , magnetic phase transformed to FeO confirmed by the peaks at $2\theta = 35.9^\circ, 41.6^\circ, 60.4^\circ,$ and 72.3° (JCPDS 89-0687). The peaks at $2\theta = 44.7^\circ$ and 65.2° (JCPDS 87-0721) suggested that magnetic phase completely transformed to $\alpha\text{-Fe}$ and $\gamma\text{-Fe}$ when pyrolysis temperature was increased to 900°C .

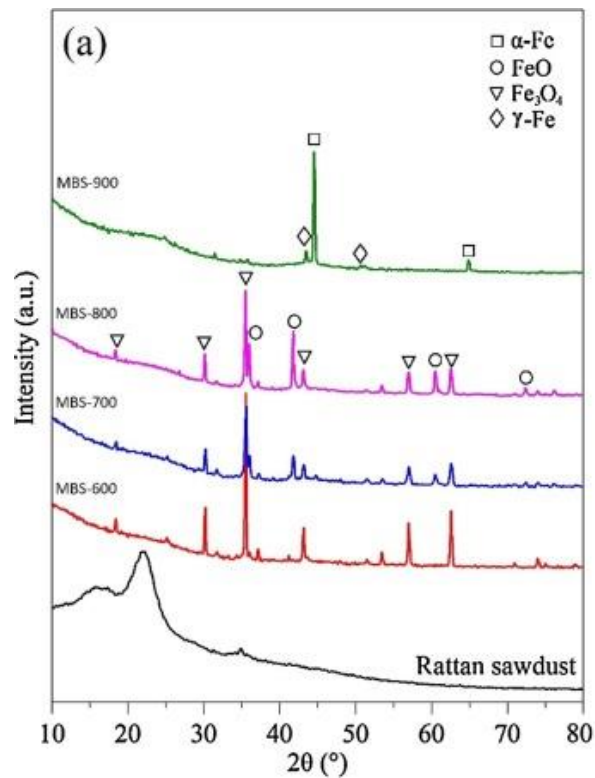


Fig. 2.8 XRD pattern of MBC [61]

From Jiang et al. [62], they used an X-ray diffractometer (XRD, MXPHF; Rigaku Corp., Tokyo, Japan) with 30 kV, 160 mA, and $\lambda = 1.5460 \text{ \AA}$ to identify magnetic phase of MBC. They found the peak of Fe, FeO, and Fe_3O_4 with the peaks located at $2\theta = 44.7^\circ$ and 65.0° (JCPDS 06-0696), $2\theta = 41.7^\circ$, 36.3° , and 61.9° (JCPDS 06-0615) 30.1° , 35.4° , 43.1° , and 56.9° (JCPDS 19-0629), respectively in MBC500 and MBC600. When pyrolysis temperature was increased to 700°C , FeO and Fe_3O_4 were completely transformed into Fe together with the formation of Fe_3C . The peaks of Fe_3C were not detected when pyrolysis temperature was increased to 800°C as shown in **Fig. 2.7**.

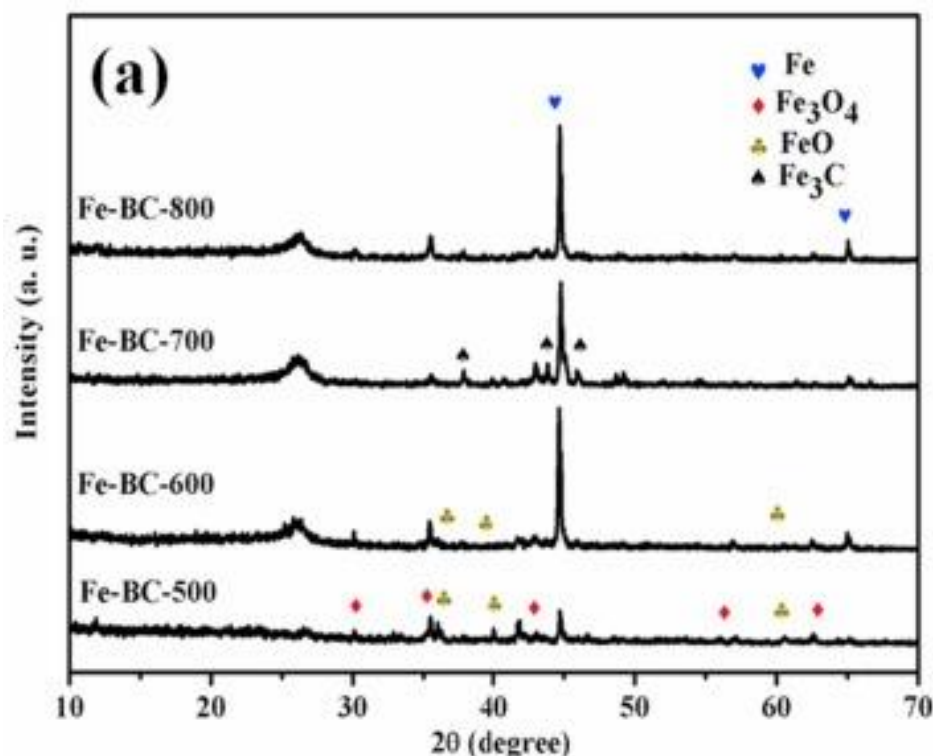


Fig. 2.9 XRD pattern of MBC [62]

2.5.3 The development model of TC adsorption capacity under various adsorption conditions

Adsorption conditions are one of important factors affecting the TC adsorption capacity. There were some studies reported on the adsorption model of TC under various adsorption conditions as follows.

Foroughi et al. [63] studied TC adsorption using $\text{Fe}_3\text{O}_4\text{-g-CN@PEI-}\beta\text{-CD}$ nanocomposite as sorbent. Adsorption conditions under various adsorption parameters including TC concentration (31-268.9 mg/L), pH (1.93-9), adsorbent dosage (1.55-13.45 g/L), temperature (23-47 °C), and contact time (3.2-20 min) were designed by central composite design (CCD). The studied factors and levels are shown in **Table 2.2**. Adsorption process was modeled by response surface methodology (RSM), boosted regression tree (BRT), and general regression neural network (GRNN) under various adsorption conditions. The result revealed BRT showed the most accurate prediction model. The order of influential factors was as follows pH > adsorbent dosage > TC concentration.

Table 2.2 The studied factors and levels [63]

Factor	Unit	Level				
		$-\alpha$ (-2)	-1	0	+1	$+\alpha$ (+2)
A-Initial TC concentration	mg/L	31	100	150	200	268.9
B-pH	-	1.93	4	5.5	7	9
C-Adsorbent dose	g/L	1.55	5	7.5	10	13.45
D-Temperature	°C	23	30	35	40	47
E-Time	min	3.2	8	11.5	15	20

Topal et al. [64] studied TC adsorption by chitosan from mussel shells. Central composite design (CCD)-based response surface methodology was used to optimize the adsorption process. Four studied factors i.e., initial TC concentration (25-125 mg/L), Time (0-80 min), adsorbent dosage (1-13 g/L), and temperature (0-40 °C). The optimal conditions for maximum adsorption efficiency were initial TC concentration of 90.5 mg/L, time of 35.9 min, temperature of 29.9 °C, and adsorbent dosage of 0.4 g.

Table 2.3 The studied factors and levels [64]

Factor	Unit	Level				
		$-\alpha$ (-2)	-1	0	+1	$+\alpha$ (+2)
A-Initial TC concentration	mg/L	25	50	75	100	125
B-Time	min	0	20	40	60	80
C-Adsorbent dosage	g	1	4	7	10	13
D-Temperature	°C	0	10	20	30	40

Nasiri et al. [65] studied TC adsorption by magnetic nanocomposite. The adsorption process was modeled and optimized by response surface methodology. CCD was used to define the experimental runs under four factors i.e., pH (3-11), initial TC concentration (4-20 mg/L), adsorbent dosage (0.05-0.25 g/L), and time (15-115 min). The maximum TC adsorption capacity was 79.45%.

Table 2.4 The studied factors and levels [65]

Factor	Unit	Level				
		- α (-2)	-1	0	+1	+ α (+2)
A-pH	-	3	5	7	9	11
B-Initial TC concentration	mg/L	4	8	12	16	20
C-Adsorbent dosage	g/ L	0.05	0.1	0.15	0.2	0.25
D-Time	min	15	40	65	90	115

However, the synthesis of MBC from agricultural waste, especially, watermelon rind by impregnation-pyrolysis for TC antibiotic adsorption and the effect of pyrolysis temperature on characteristics of MBC is still limited. It would be beneficial to develop TC adsorption model of MBCs derived from watermelon rind under various adsorption conditions based on RSM. Moreover, it would be beneficial to develop TC adsorption model using ML under characteristics of the adsorbent with updated data.

CHAPTER 3 METHODOLOGY

This research, this chapter would be divided into 5 parts. The first part is chemicals and materials. The second part is synthesis of MBC. The third part is characterization techniques. The fourth part is adsorption experiments, and the last is the development of empirical model.

3.1 Chemicals and materials

A batch of watermelon rind was collected from a single local market in Bangkok, Thailand for ensuring the whole investigation. Morphology of watermelon rind with 1300X magnification as shown in **Fig. 3.1**. Elemental composition of watermelon rind (dry basis) is listed in **Table 3.1**. Iron (III) chloride hexahydrate (99% purity, AR grade, QReC) was used to impregnate on watermelon rind. Nitrogen (99.6% ultra-high purity industrial grade, Linde) was used to make pyrolysis system fully with inert gas. Tetracycline ($\geq 98\%$ purity, Sigma-Aldrich) was used for adsorption experiment.

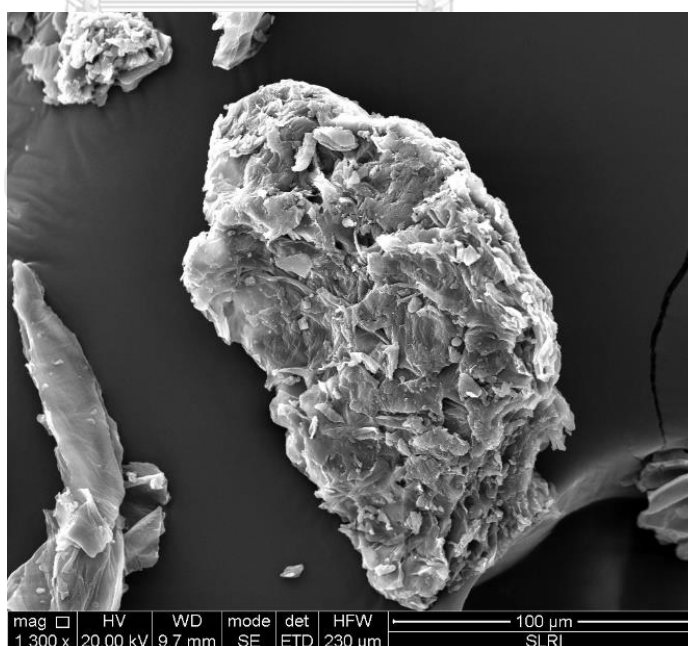


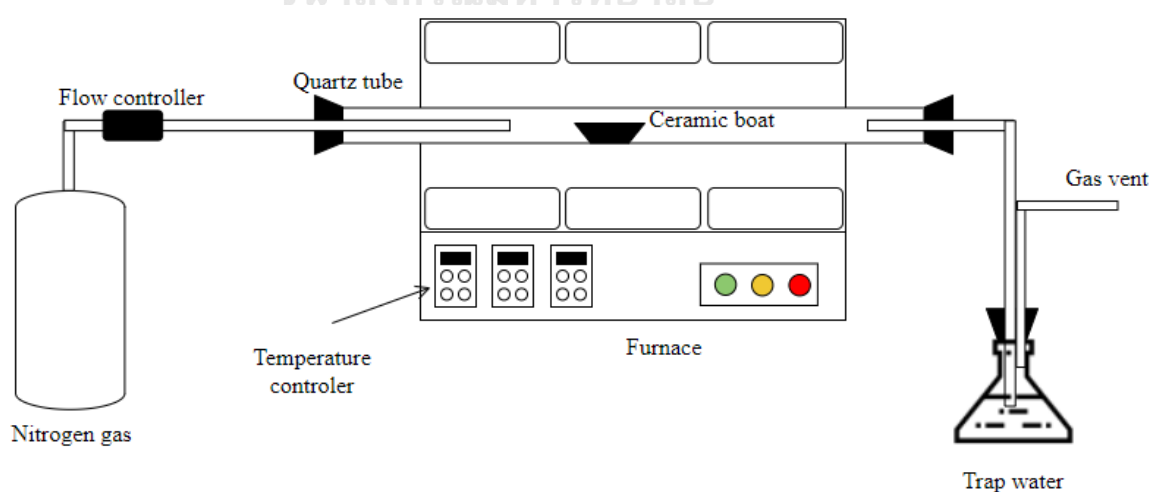
Fig. 3.1 Morphology of watermelon rind

Table 3. 1 The elemental content of watermelon rind

Element	Percentage composition (%)
Carbon	35.17
Hydrogen	5.24
Nitrogen	2.20
Oxygen	57.39

3.2 Synthesis of MBC

Watermelon rind was cut, dried, and sieved to a size less than 300 μm . A particulate sample of watermelon rind was immersed in FeCl_3 solution with a 2:1 weight ratio of FeCl_3 to watermelon rind for 2 h with magnetic stirring, then the solid residue was filtered and dried at 80 $^\circ\text{C}$ overnight. Then, FeCl_3 -impregnated sample was pyrolyzed from room temperature with a heating rate of 8 $^\circ\text{C}/\text{min}$ to designated temperatures (600, 700, 800, and 900 $^\circ\text{C}$), then, hold for 2 h under N_2 atmosphere (0.05 L/min) using electrical quartz tube furnace. Experimental schematic is shown in **Fig. 3.2**. After being cooled down, the resultant sample was labeled as MBCT, where T represented the pyrolysis temperature ($T=600, 700, 800, \text{ and } 900^\circ\text{C}$).

**Fig. 3.2** The experimental schematic of MBC synthesis

3.3 Characterization techniques

3.3.1 Surface morphology of MBCs

Surface morphology of MBCs was observed by environmental scanning electron microscope (Quanta450, FEI, Czech), which showed in **Fig.3.3**. SEM images were performed with 1,300X magnification.



Fig. 3.3 Environmental scanning electron microscope model Quanta450

3.3.2 Chemical composition

The chemical composition of dried watermelon rind and MBCs were analyzed by an elemental analyzer (Thermo flash 2000, Thermo Fisher Scientific), which showed in **Fig 3.4**. The oxygen content (O%) was calculated by subtracting total C%, H%, and N% from 100%.



Fig. 3.4 Element analyzer model Thermo flash 2000

3.3.3 Specific surface area and pore volume of MBCs

The specific surface area and pore volume of MBCs were analyzed by N₂ adsorption/desorption isotherms (ASAP2460, Micromeritics, Thailand), which showed in **Fig. 3.5**. First, samples were degassed at 300 °C for 5 h. Then, degassed samples were taken to measure N₂ adsorption/desorption. The data is shown in the form of BET isotherm, which is relationship between gas adsorbed and relative pressure. Specific surface area and total pore volume were calculated by BET equation.



Fig. 3.5 Surface area and porosimetry analyzer model ASAP2460

3.3.4 Surface functional groups of MBCs

The surface functional groups of MBCs were identified by FTIR spectrometer (Nicolet 6700, Thermo Fisher Scientific, USA), which showed in **Fig.3.6**. Wavelength was studied in the range of 500 cm^{-1} to 3700 cm^{-1} .

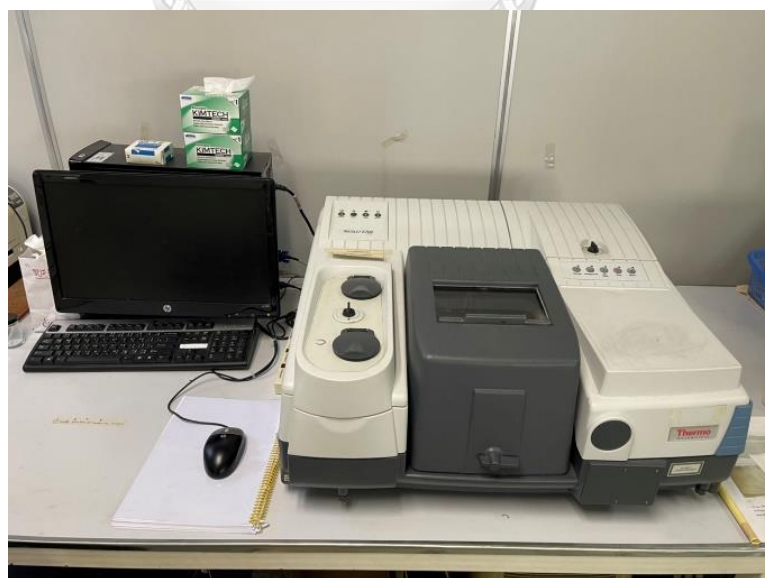


Fig. 3.6 FTIR spectrometer model Nicolet 6700

3.3.5 Crystallinity of MBCs

The crystallinity of MBCs was identified by Raman spectroscopy (NTEGRA spectra, NT-MDT, Russia), which showed in **Fig. 3.7**. Red laser with a wavelength of 632.8 nm was used and Raman shift was studied in the range of 1000 to 2000 cm^{-1} .

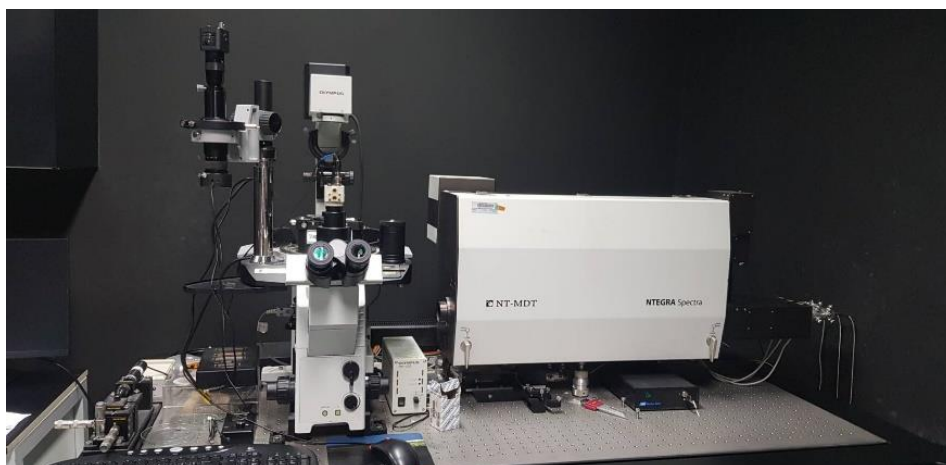


Fig. 3. 7 Raman spectroscopy model NTEGRA spectra

3.3.6 Magnetic property of MBCs

The magnetic moment of MBCs was investigated by vibrating sample magnetometer (7404, Lake Shore, USA), which showed in **Fig. 3.8**. The magnetic field was studied between -6000 G and +6000 G.

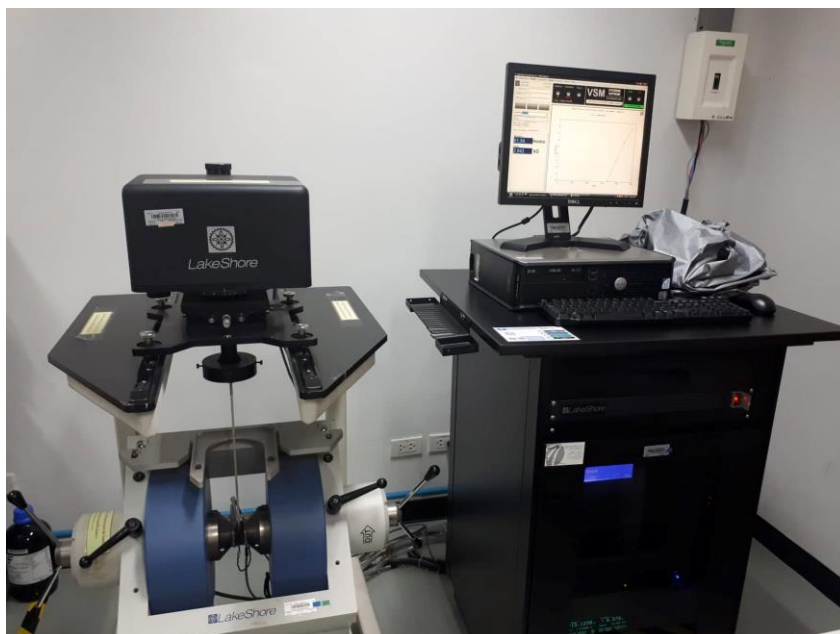


Fig. 3.8 Vibrating sample magnetometer model 7404

3.3.7 Magnetic phases of MBCs

The magnetic phases of MBCs were identified by x-ray diffraction spectroscopy (D8 Discover, Bruker), which showed in **Fig. 3.9**. XRD pattern was recorded in the 2θ range from 10° to 80° (Cu, 40 kV, 40 mA) with scanning speed of $10^\circ/\text{min}$.



Fig. 3.9 X-ray diffraction spectroscopy model D8 Discover

3.4 Adsorption experiments

Adsorption kinetic experiment was carried out with conditions as follows 50 mL of TC solution with initial concentration of 40 mg/L was added in 60 mL amber glass bottle, and then MBC dosage of 0.3 g/L was added. The bottles were placed in an orbital shaker (NR-201M, N-TER) at 120 rpm. shaken up for 180 min, the solution was periodically taken off for TC concentration measurement using UV-Vis spectrophotometer (UV-2600 240V EN, Shimadzu, Japan) at a wavelength of 359 nm. Adsorption isotherm experiments were carried out by adding 50 mL of TC solution with different initial concentrations varied 10-100 mg/L in amber glass bottle, then MBC dosage of 0.3 g/L was added. The amber glass bottle was placed in the orbital shaker at 120 rpm. shaken up for 3 hr to reach equilibrium.

The TC adsorption capacity was calculated based on equation below:

$$q = \frac{(C_i - C_t)}{C_0} \quad (2)$$

Where,

q is TC adsorption capacity (mg/g).

C_i is initial TC concentration (mg/L).

C_e is TC concentration at time t (mg/L).

C_0 is adsorbent dosage (g/L).

The effect of solution pH on TC adsorption capacity of MBC was examined between 3 and 11. The solution pH was adjusted by adding 0.1M of HCl solution or 0.1M of NaOH solution into 50 mL of TC solution with initial TC concentration of 20 mg/L, then 15 mg of MBC900 was added. The amber glass bottles were placed in orbital shaker at 120 rpm. shaken up for 180 min, then TC solutions were taken to measure concentration.

The reusability of MBC was investigated by adsorption-desorption process. The 15 mg of MBC900 was added into 40 mg/L and 50 mL of TC solution. Then the amber glass bottle was placed in orbital shaker at 120 rpm. After 180 min, the

solution was taken off for TC concentration measurement and MBC900 was separated by external magnet. The MBC900 was immersed in 0.5M NaOH solution and shaken for 5 h, then wash MBC900 with DI water until neutral. The above process was repeated in five cycles.

3.5 Development of model

3.5.1 Development of empirical model based on RSM

MBC900 was employed as adsorbent for studying development of empirical model. CCD was used to define experimental runs using Design Expert 11 software to model TC adsorption capacity under studied factors i.e., A-initial TC concentration, B-adsorbent dosage, C-solution pH, and D-contact time. The studied factors and levels are provided in **Table 3.2**. The experimental runs are provided in **Table 3.3**. The CCD design contains five coded levels of $-\alpha$, -1, 0, +1, $+\alpha$, representing lower axial, low, medium, high, and upper axial points, respectively. Where α is calculated by $\alpha = 2^{\frac{k}{4}}$ which k is the number of factors. TC adsorption capacities were fitted with a second-order model of RSM as described in equation (1) to investigate the relationship between the factors. Analysis of variance (ANOVA) was used to investigate the quality of the model and estimate the significance of each term in the model.

จุฬาลงกรณ์มหาวิทยาลัย
CHULALONGKORN UNIVERSITY

Table 3.2 The studied factors and levels used to design experimental runs

Factor	Unit	Level				
		$-\alpha$ (-2)	-1	0	+1	$+\alpha$ (+2)
A-Initial TC concentration	mg/L	20	40	60	80	100
B-Adsorbent dosage	g/L	0.1	0.2	0.3	0.4	0.5
C-Solution pH	-	3	5	7	9	11
D-Time	Min	15	30	45	60	75

Table 3.3 Experimental runs designed based on CCD

Run	Initial TC concentration (mg/g)	Adsorbent dosage (g/L)	Solution pH	Time (min)
1	60	0.3	7	45
2	60	0.3	11	45
3	80	0.2	5	60
4	40	0.2	9	60
5	80	0.2	9	30
6	40	0.2	5	60
7	60	0.3	7	45
8	20	0.3	7	45
9	80	0.4	9	30
10	40	0.4	9	30
11	40	0.2	9	30
12	60	0.3	7	45
13	80	0.4	5	60
14	60	0.3	7	75
15	60	0.3	3	45
16	80	0.4	5	30
17	40	0.4	5	30
18	40	0.4	5	60
19	40	0.4	9	60
20	100	0.3	7	45
21	60	0.3	7	45
22	80	0.2	9	60
23	60	0.3	7	45
24	60	0.1	7	45
25	60	0.3	7	45
26	60	0.3	7	45
27	40	0.2	5	30
28	80	0.4	9	60
29	60	0.5	7	45
30	60	0.3	7	15
31	80	0.2	5	30

3.5.2 Development of semi-empirical model based on ML

The 100 different adsorbents for TC adsorption were collected from 37 journal publications including data from this research. The data of characteristics of the adsorbents and references are summarized in **Table F.1**. The data of S_{BET} , C%, H/C, (O+N)/C, and initial TC concentration toward TC adsorption capacity of 100 different adsorbents were collected. The data were normalized by z-score as shown in following equation.

$$z_i = \frac{x_i - \mu}{\sigma} \quad (3)$$

Where, z_i is normalized data, x_i is originally data, μ is average of data, and σ is standard deviation of data for each variable. The normalized data were randomly split into training set and testing set in a ratio of 85:15. RF, Catboost, and BRT algorithms were applied to the development of semi-empirical model using Python. The source codes are provided in **Appendix G**.

CHAPTER 4 RESULTS AND DISCUSSION

This chapter is divided into three parts. Firstly, effect of pyrolysis temperature on product yield and characteristics of pyrolyzed products including morphology, chemical composition, specific surface area (S_{BET}), total pore volume (V_P), surface functional groups, and crystallinity were analyzed. Magnetic phase and magnetic moment of all pyrolyzed products were analyzed to confirm their magnetic property could facilitate separation and recycling processes. Secondly, the pyrolyzed products obtained from different pyrolysis temperatures were employed for TC adsorption for examining their adsorption kinetics, isotherm, effect of initial pH, and reusability. Finally, the models of TC adsorption capacity based on RSM and ML were developed.

4.1 Effects of pyrolysis temperature on characteristics of pyrolyzed products

Morphology of as-synthesized samples was observed by SEM as shown in **Fig. 4.1**. Similar porous morphology of all pyrolyzed products could be observed. N_2 adsorption/desorption method was used for quantitative analysis of specific surface area (S_{BET}), pore volume (V_P), and pore size distribution of pyrolyzed products. **Table 4.1** exhibited that with pyrolysis temperature of 600 °C, pyrolyzed sample (MBC600) possesses the lowest S_{BET} of 58.14 m²/g and V_P of 0.046 cm³/g. However, an increase in pyrolysis temperature could enhance both S_{BET} and V_P of MBC. Correspondingly, at temperature of 900 °C, pyrolyzed sample (MBC900) possesses the highest S_{BET} of 401.11 m²/g and V_P of 0.236 cm³/g. The average pore size diameter (D_{avg}) of MBC600, MBC700, MBC800, and MBC900 were 3.19, 2.33, 2.31, and 2.36 nm, respectively. BET isotherm of all pyrolyzed sample reveals isotherm type IV as shown in **Fig. 4.2**, suggesting S_{BET} and V_p that reported in **Table 4.1** are mesoporous. However, pore size distribution of all synthesized MBCs as shown in **Fig. 4.3** reveals pyrolyzed products consists of both mesoporous (4nm) and microporous (≤ 2 nm)[66]. From these results, it should be noted that an increase in pyrolysis temperature would enhance S_{BET} along with mesopore and micropore of resultant products.

Meanwhile, product yield of pyrolyzed products decreased from 35.51 % to 26.76 % with pyrolysis temperature increased from 600 to 900 °C as shown in **Table 4.1**. These results would be concluded that such porous structure would be created from the decomposition of lignocellulosic components within the watermelon rind precursor at an elevated temperature[67, 68]. An increase in the pyrolysis temperature would enhance the decomposition, which would result in a decreased product yield of the resultant products.

Similar trend of effect of pyrolysis temperature on product yield of magnetic biochar was also observed. Hu et al. [61] reported that product yields of as-synthesized magnetic biochar were 34.49, 31.71, 24.82, and 25.30% when using pyrolysis temperatures of 600, 700, 800, and 900 °C.

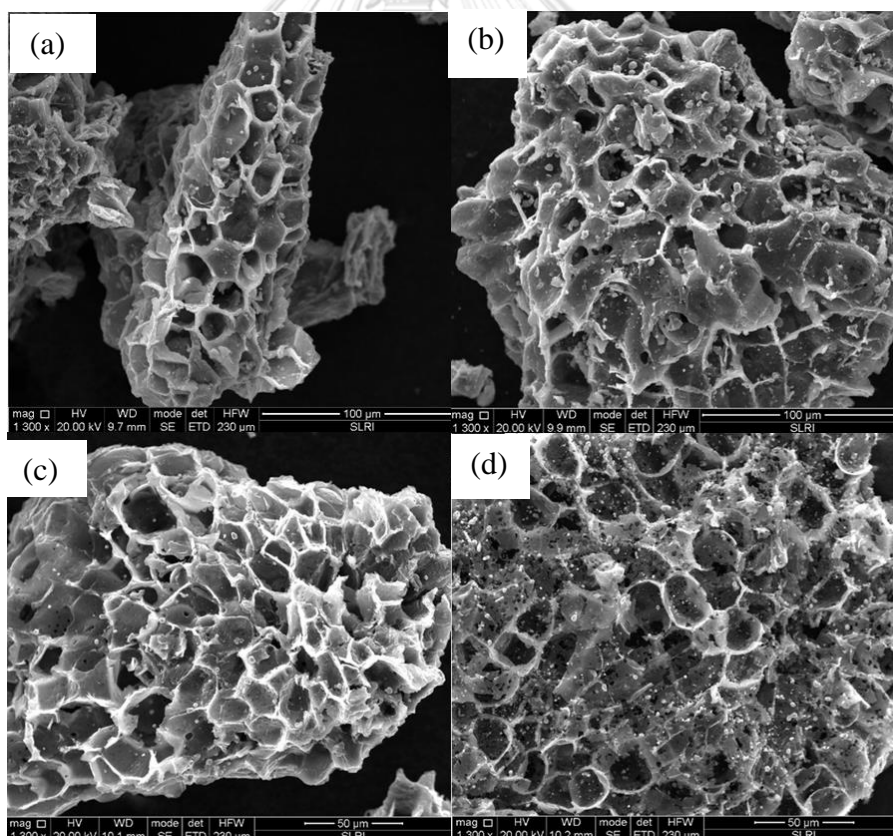
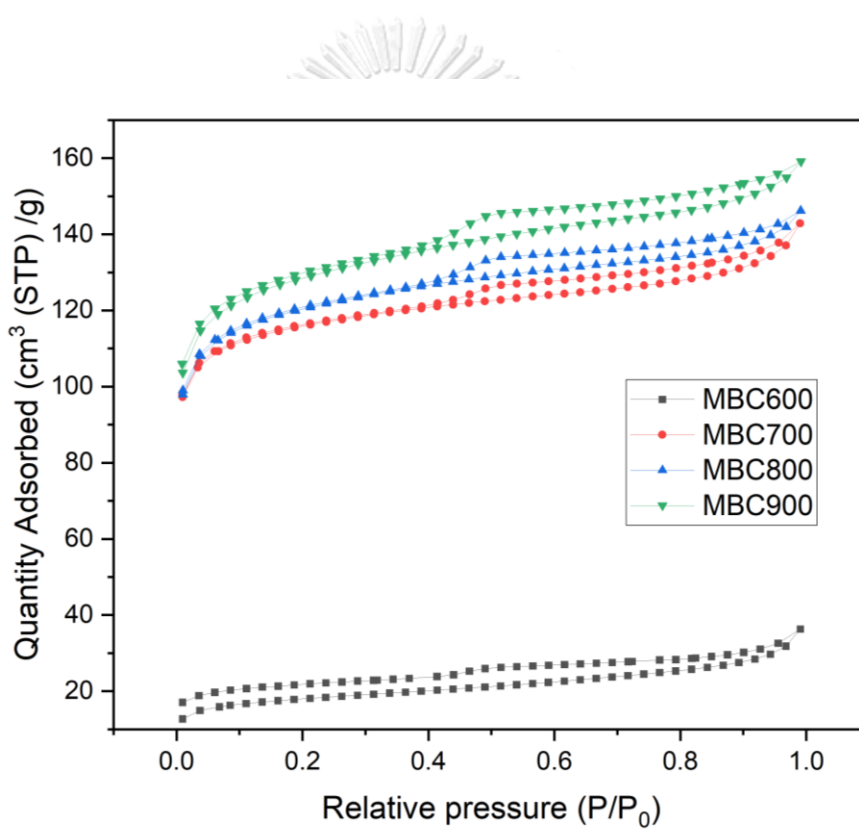


Fig. 4.1 SEM images of pyrolyzed samples obtained at pyrolysis temperature of (a) 600 (b) 700 (c) 800 (d) 900 °C

Table 4.1 S_{BET} , V_p , and yield of different MBC samples

Sample	S_{BET} (m ² /g)	V_p (cm ³ /g)	D_{avg} (nm)	Yield (%)
MBC600	58.14	0.046	3.19	33.51 ± 0.94
MBC700	358.05	0.208	2.33	30.93 ± 0.40
MBC800	374.81	0.216	2.31	28.30 ± 1.16
MBC900	401.11	0.236	2.36	26.76 ± 1.31

**Fig. 4. 2** BET isotherm of pyrolyzed samples

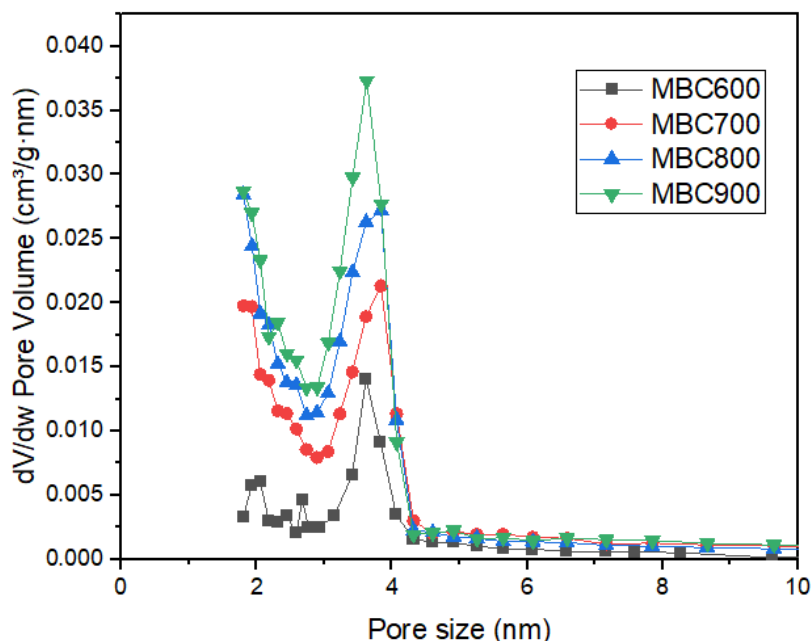


Fig. 4. 3 Pore size distribution of pyrolyzed samples

For employed MBC as the adsorbent chemical composition, surface functional groups, and crystallinity of MBC were investigated. The chemical composition of MBC samples is shown in **Table 4.2**. When pyrolysis temperature was increased from 600 °C to 900 °C, the C content of MBC samples significantly increased from 64.31 to 67.31 % meanwhile the O content of MBC samples decreased from 32.28 to 30.98 %. These results indicate that an increase in pyrolysis temperature enhances the degree of carbonization, dehydration reaction, and decomposition of oxygenated bonds[69]. The ratio of O/C and (O+N)/C represent the polarity of the MBC. The pyrolysis temperature significantly affects to O/C ratio of MBC, which decreased from 0.37 to 0.34 when pyrolysis temperature increased from 600 °C to 900 °C. A similar trend in O/C ratio could be observed in (O+N)/C ratio, indicating a more hydrophobic surface of MBC at higher pyrolysis temperature [70].

A similar trend of chemical composition with pyrolysis temperature was reported in Wang et al. work [71]. It was reported that the C content of rice straw biochar increased from 45.22% to 56.00% while O content decreased from 23.41 % to 11.38 % when pyrolysis temperature was increased from 300 °C to 700 °C due to an increase in degree of carbonization.

Table 4.2 Chemical composition of MBCs

Sample	C (%)	H (%)	N (%)	O (%)	O/C	(O+N)/C
MBC600	64.31±0.25	1.50±0.08	1.90±0.24	32.28±0.05	0.37	0.40
MBC700	64.72±0.06	0.92±0.10	1.60±0.02	32.76±0.13	0.38	0.40
MBC800	66.83±0.25	0.60±0.11	1.12±0.02	31.46±0.11	0.35	0.37
MBC900	67.31±0.54	0.91±0.12	0.81±0.00	30.98±0.30	0.34	0.35

Surface functional groups of pyrolyzed products were investigated by FTIR spectrometer. FTIR spectra of all pyrolyzed samples are shown in **Fig. 4.3**. Characteristic peak at 3450 cm^{-1} represents O-H stretching vibration [72]. The peak at 1100 cm^{-1} corresponded to C-O-C stretching [73]. Additionally, characteristic peak of O-H stretching vibration of pyrolyzed sample synthesized at higher pyrolysis temperature is distinctly smaller, indicating the acceleration of dehydration reaction at high temperature [67], which is consistent with the chemical composition of MBC (**Table 4.2**). The upper peak at 2900 cm^{-1} appeared maybe due to impurity in the sample chamber. The upper peak at 2300 cm^{-1} is assigned to CO_2 peak from the difference of CO_2 in sample and background. These results would also support the decrease in product yield (**Table 4.1**).

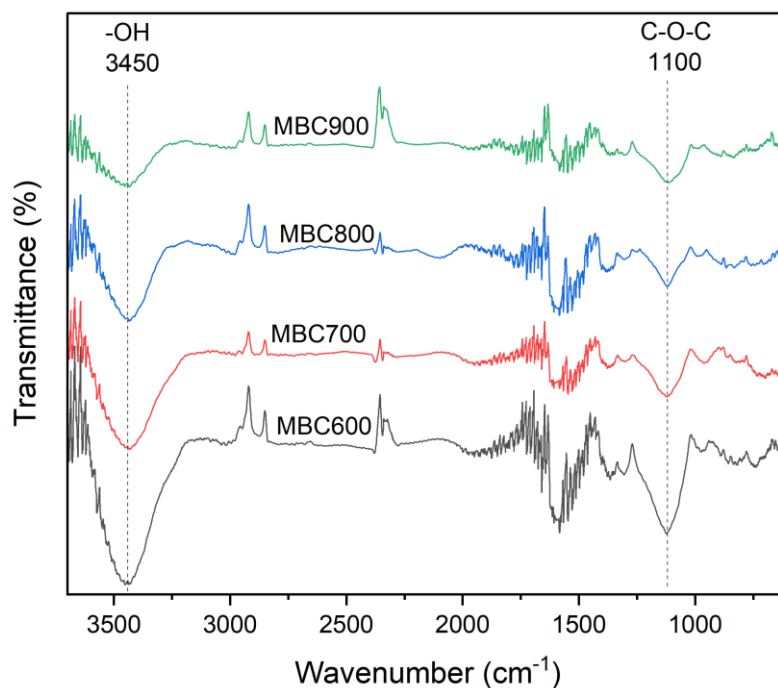


Fig. 4.4 FTIR spectra of different MBC samples

Raman spectroscopy was employed for investigating crystallinity of pyrolyzed products, especially, sp^2 at Raman shift around 1600 cm^{-1} , which is graphitic carbon, and sp^3 at Raman shift around 1300 cm^{-1} , which is amorphous carbon[74]. Raman spectra of all pyrolyzed samples are shown in **Fig. 4.4**. The intensity of sp^3 carbon representing amorphous carbon at Raman shift around 1300 cm^{-1} (also known as D-band) and the intensity at Raman shifts around 1600 cm^{-1} (G-band) could be detected in all MBC samples. When pyrolysis temperature was increased from $600\text{ }^\circ\text{C}$ to $900\text{ }^\circ\text{C}$, I_G to I_D ratio representing degree of graphitic carbon to amorphous carbon (I_G/I_D) increased from 0.80 to 0.86. The calculation of I_G/I_D ratio was obtained from curve fitting of Raman spectra as shown in **Fig. D1**. These results would be ascribed that an increase in pyrolysis temperature would enhance degree of graphitization.

There were some studies on effect of pyrolysis temperature on Raman spectra of magnetic biochar. Jiang et al. [62] found that I_G/I_D of magnetic sawdust biochar increased from 1.06 to 1.27 when pyrolysis temperature was increased from $500\text{ }^\circ\text{C}$ to $800\text{ }^\circ\text{C}$. Due to the increase in degree of graphitization at high pyrolysis temperature.

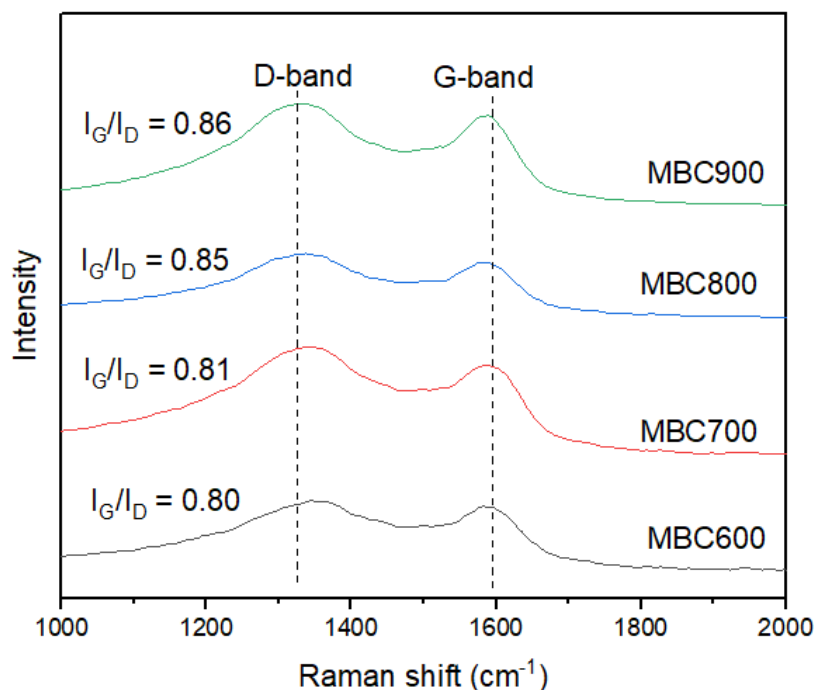


Fig. 4.5 Raman spectra of pyrolyzed samples

Magnetic phases of all pyrolyzed samples were identified by X-ray diffraction as shown in **Fig. 4.5**. The pyrolyzed sample obtained at pyrolysis temperature of 600 °C (MBC600) exhibited magnetic phase of Fe₃O₄ confirmed by peaks around $2\theta = 18.2^\circ, 30.0^\circ, 35.4^\circ, 43.0^\circ, 56.9^\circ, 62.5^\circ$ (JCPDS 89-0688)[75]. At pyrolysis temperature of 700 °C, the magnetic phases of resultant product (MBC700) transformed to FeO and α -Fe confirmed by peaks around $2\theta = 35.9^\circ, 41.6^\circ, 60.4^\circ$ (JCPDS 89-0687), and $2\theta = 44.7^\circ, 65.2^\circ$ (JCPDS 87-0721) respectively [61, 76]. However, when pyrolyzed temperature was increased from 800 to 900 °C (MBC800 and MBC900), the magnetic phase of resultant sample is completely transformed to α -Fe.

According to XRD pattern of as-synthesized product, the transformation of magnetic phase could be described as follow. First FeCl₃ reacts with water and then form Fe₂O₃ as given in Equation (3) and (4)[77]. When pyrolysis temperature is higher than 570 °C, Fe₂O₃ could be reduced by CO and H₂ to form Fe₃O₄, FeO, and Fe in three steps as shown in Equations (5), (6), (7), (8), (9), and (10)[78].

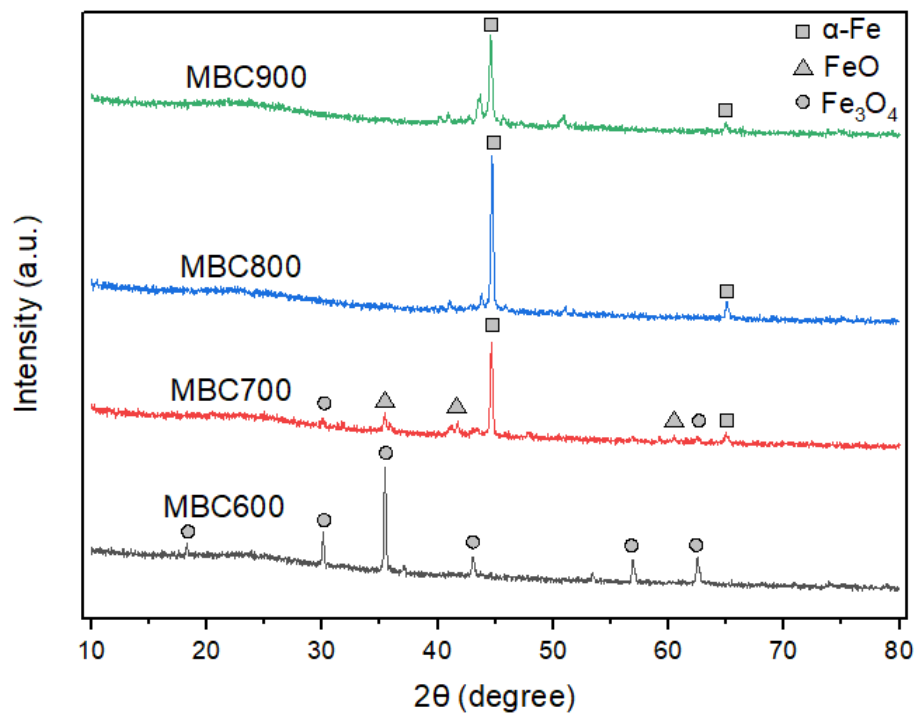
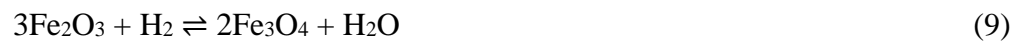


Fig. 4.6 Magnetic phases of pyrolyzed samples

For investigating magnetic property of all pyrolyzed samples, external magnet and vibrating sample magnetometer were employed. Magnetic moment of pyrolyzed samples is exhibited in **Fig. 4.6**. All pyrolysis products exhibited ferromagnetic

behavior due to originality of magnetic phase (Fe_3O_4 , FeO , and $\alpha\text{-Fe}$) with non-nano-size [79]. The size analysis of $\alpha\text{-Fe}$ in MBC900 from ImageJ program revealed mean diameter of $\alpha\text{-Fe}$ is $2.07\ \mu\text{m}$ (data are provided in **Table B.1**). The pyrolyzed sample obtained at pyrolysis temperature of $600\ ^\circ\text{C}$ (MBC600) possessed low saturation magnetization (M_s) value of $4.49\ \text{emu/g}$ and high coercivity (H_c) of $53.93\ \text{G}$. However, pyrolyzed samples obtained at pyrolysis temperatures of 800 and $900\ ^\circ\text{C}$ possessed higher M_s values and lower H_c values as shown in **Table 4.2**. The difference in M_s may be due to the purity or the size of magnetic particles being different [80]. The higher magnetic saturation (M_s) value of MBC, the faster separation of MBC could be obtained when induced by an external magnet. After removing the external magnet, MBC with low H_c value will be able to not accumulate [81]. **In Fig. 4.7a**, MBC900 was added into DI water and then used external magnet to induce MBC sample. It was found that MBC could be easy and completely separated by the external magnet as shown in **Fig. 4.7b**. Based on these results, such magnetic property of the MBC samples would be beneficial for the recovery of sorbents after treatment process. These results could be implied that pyrolysis of FeCl_3 -impregnated watermelon rind could provide biochar with magnetic property.



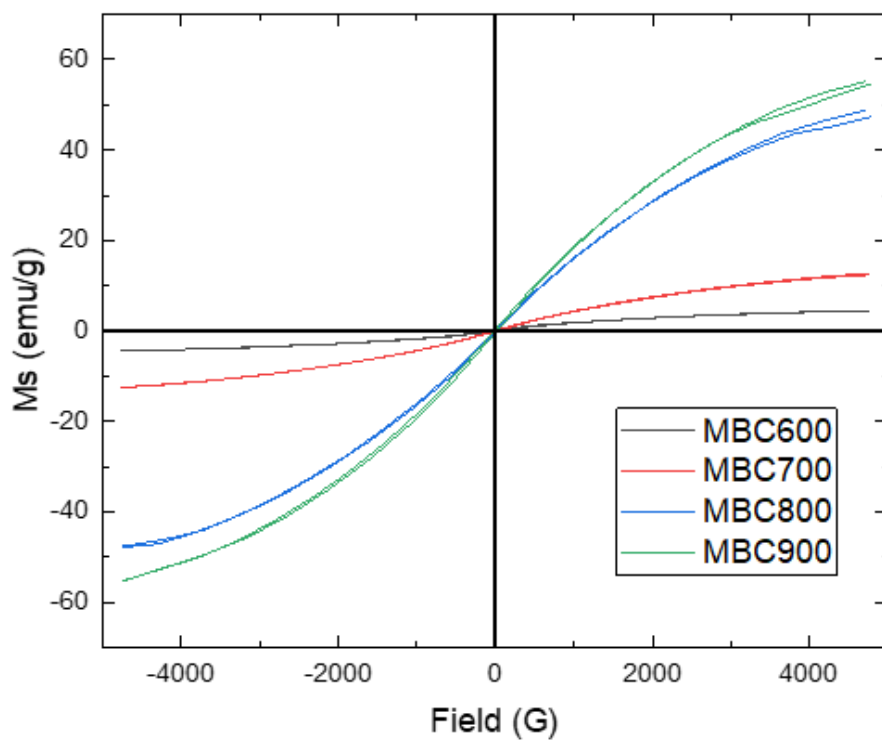


Fig. 4.7 Magnetic hysteresis of pyrolyzed samples

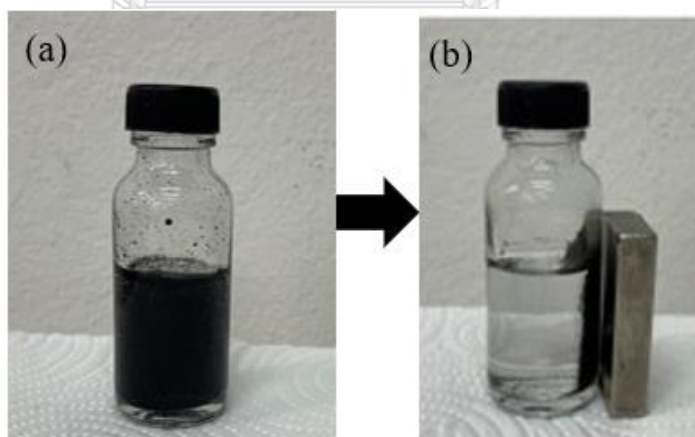


Fig. 4.8 Dispersion of MBC900 (a) before induced by external magnet (b) induced by external magnet

Table 4.3 Saturation magnetization (M_s) and Coercivity (H_c) of pyrolyzed samples

Sample	M_s (emu/g)	H_c (G)
MBC600	4.49	53.95
MBC700	12.60	29.12
MBC800	48.32	15.10
MBC900	55.29	17.81

4.2 Adsorption experiments

MBCs were employed as adsorbents for investigating TC adsorption experiments. Adsorption kinetics and isotherm were studied for understanding adsorption behavior. Influences of initial pH on TC adsorption capacity and reusability test of MBC were also conducted.

4.2.1 Tetracycline adsorption kinetic of MBCs

Adsorption kinetic is used to study the reaction rate and adsorption mechanisms. The relationship between adsorption amount and contact time is exhibited in **Fig. 8a**. The fast adsorption could be observed in the first 30 min. However, after 30 min, the adsorption is slower. This is because the remaining adsorption site is decreased due to the occupation of TC. Additionally, adsorption process could reach equilibrium within 60 min. The adsorption process was studied by two kinetic models, i.e., pseudo-first-order kinetic model and pseudo-second-order kinetic model, which are expressed in equations (11) and (12) [82]:

Pseudo-first-order kinetic equation:

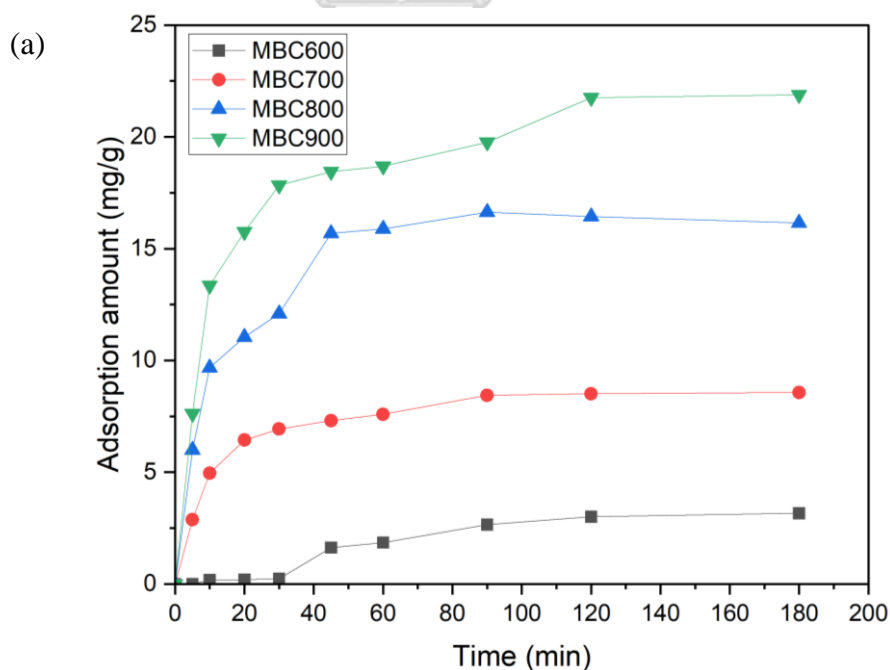
$$\ln(q_e - q_t) = \ln(q_e) - k_1 t \quad (12)$$

Pseudo-second-order kinetic equation:

$$\frac{t}{q_t} = \frac{1}{k_2 q_e^2} + \frac{t}{q_e} \quad (13)$$

Where t is contact time (min), q_t is TC adsorption amount at time t ($\text{mg}\cdot\text{g}^{-1}$), q_e is TC equilibrium concentration ($\text{mg}\cdot\text{g}^{-1}$), k_1 , and k_2 is rate constant (min^{-1} for pseudo-first-order, $\text{g}\cdot\text{mg}^{-1}\cdot\text{min}^{-1}$ for pseudo-second-order).

Linear plot of $\ln(q_e - q_t)$ versus t is shown in **Fig. 4.8b**. The slope of the plot was used to calculate k_1 and the intercept value was used to calculate q_e which are exhibited in **Table 4.4**. Meanwhile, linear plot of t/q_t versus t is shown in **Fig. 4.8c**. The slope of the plot was used to calculate q_e and the intercept and q_e values were used to calculate k_2 which are also exhibited in **Table 4.4**. The linear coefficient of pseudo-first-order kinetic model ($R^2 = 0.99$) was higher than pseudo-second-order kinetic model ($R^2 = 0.96$) in MBC600. However, in the case of MBC700, MBC800, and MBC900, linear coefficient of pseudo-second-order kinetic model ($R^2 = 0.99$) was higher than pseudo-first-order kinetic model ($R^2 = 0.89-0.92$) indicating the adsorption depends on concentration of two molecules, which are TC and active sites of MBC.



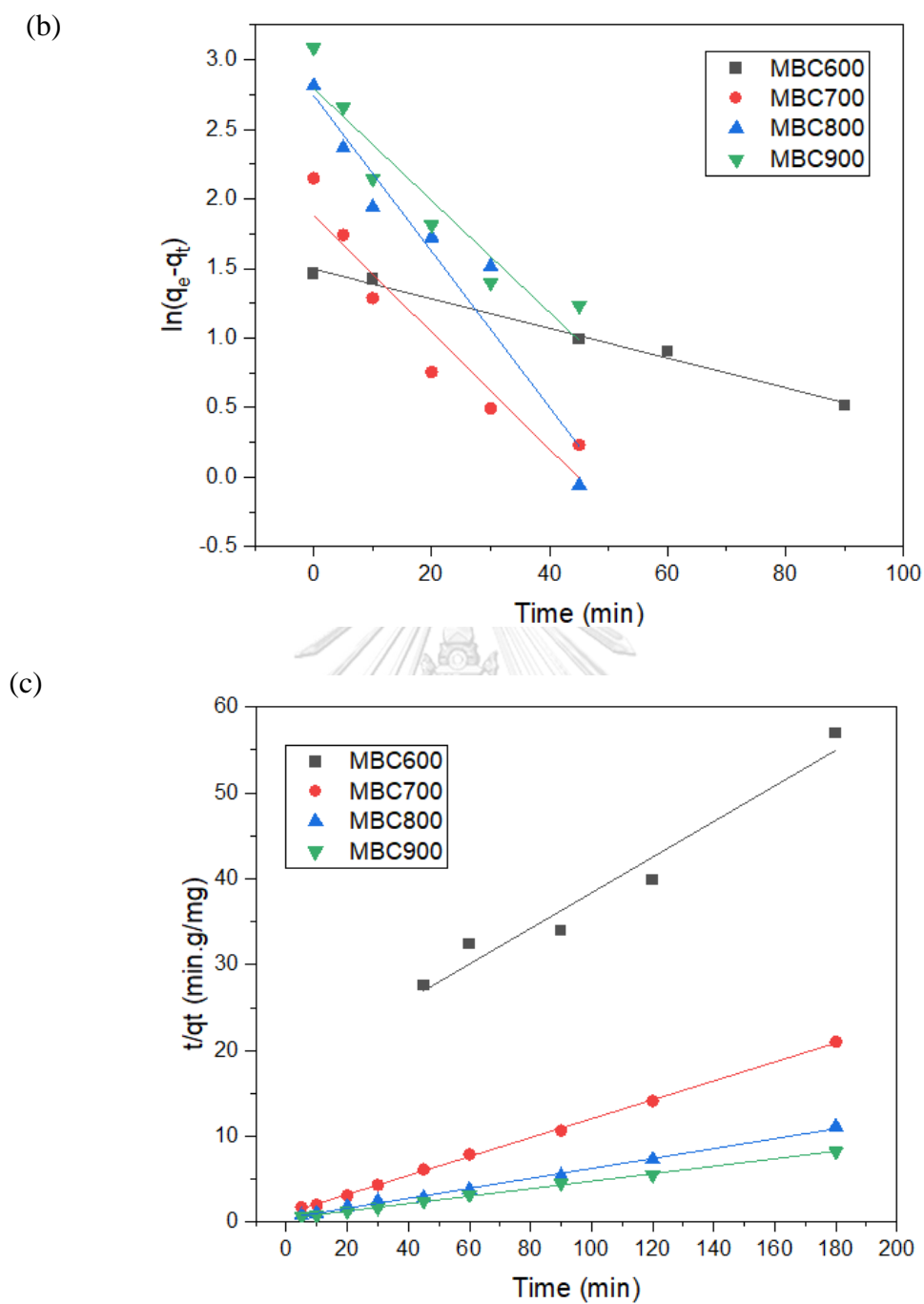


Fig. 4.9 (a) Adsorption kinetics, (b) Linearized pseudo-first-order kinetic model, and (c) Linearized pseudo-second-order kinetic model

Table 4.4 Adsorption kinetics parameter

Sample	Pseudo-first-order model			Pseudo-second-order model		
	k_1 (min^{-1})	q_e (mg.g^{-1})	R^2	k ($\text{g.mg}^{-1}\text{min}^{-1}$)	q_e (mg.g^{-1})	R^2
MBC600	0.025	4.46	0.99	0.002	4.82	0.96
MBC700	0.097	6.54	0.91	0.012	9.08	0.99
MBC800	0.129	15.52	0.92	0.007	17.28	0.99
MBC900	0.093	16.32	0.89	0.004	22.96	0.99

4.2.3 Tetracycline adsorption isotherm of MBCs

Adsorption isotherm was performed to study adsorption behavior. The relationship between adsorption capacity (q_e) and concentration of adsorbate (C_e) at equilibrium is shown in **Fig. 4.9**. The q_e values of all MBCs increased with an increase in C_e values. The adsorption equilibrium data were fitted by Linearized Langmuir and Freundlich isotherm models, which are expressed in equations (13) and (14) [83]:

Langmuir isotherm equation:

$$\frac{C_e}{q_e} = \frac{1}{q_m \times K_L} + \frac{C_e}{q_m} \quad (14)$$

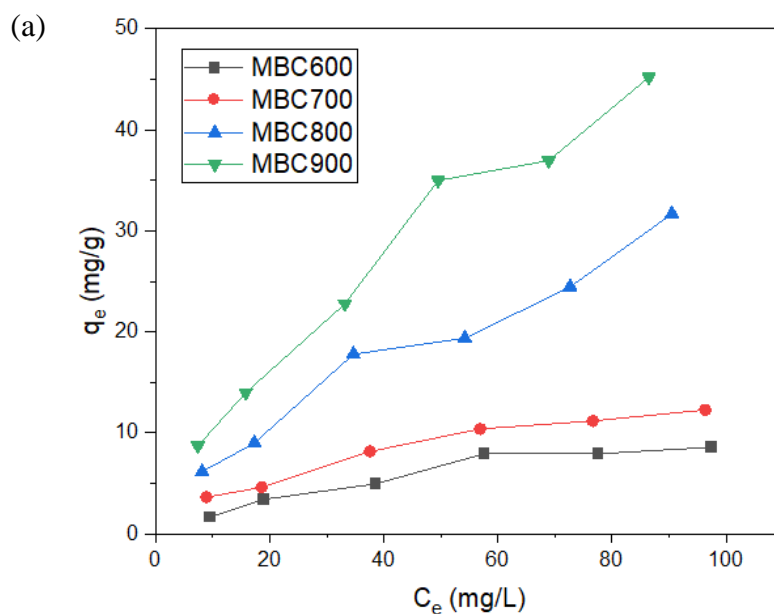
Freundlich isotherm equation:

$$\ln q_e = \frac{1}{n} \ln C_e + \ln K_f \quad (15)$$

Where C_e is concentration of adsorbate at equilibrium (mg/L), q_e is adsorption capacity at equilibrium (mg/g), q_m is maximum adsorption capacity (mg/g), K_L is Langmuir isotherm constant, K_f and n are Freundlich isotherm constant.

Linear plots of C_e/q_e versus C_e and $\ln q_e$ versus $\ln C_e$ are shown in **Fig. 9(b-c)**. The q_m values and adsorption isotherm constant are exhibited in **Table 4.5**, which are

calculated from the slope of the plot. The q_m values of MBC600, MBC700, MBC800, and MBC900 were 14.42, 17.59, 52.25, and 77.60 mg/g respectively. An increase in q_m values possesses a positive trend with S_{BET} . MBC with higher S_{BET} could provide more active site for adsorption of TC[23]. However, previous works reported that π - π electron donor–acceptor (EDA) interaction was the main mechanism of TC adsorption [4, 84]. In this work, MBC700, MBC800, and MBC900 possessed graphitic carbon which could be electron donors while TC could be electron acceptors (π - π EDA interaction) [4, 84]. Raman spectra (**Fig. 4.4**) investigated that an increase in pyrolysis temperature increased degree of graphitization. Therefore, π - π EDA interaction was promoted, which would enhance adsorption capacity. Additionally, the higher linear coefficient of Freundlich isotherm model ($R^2=0.96-0.99$) than Langmuir isotherm model ($R^2=0.84-0.97$) suggests the adsorption process based on heterogenetic adsorption site [85]. It is consistent with the results of Raman spectra (**Fig. 4.4**) that MBC possesses amorphous and graphitic carbon.



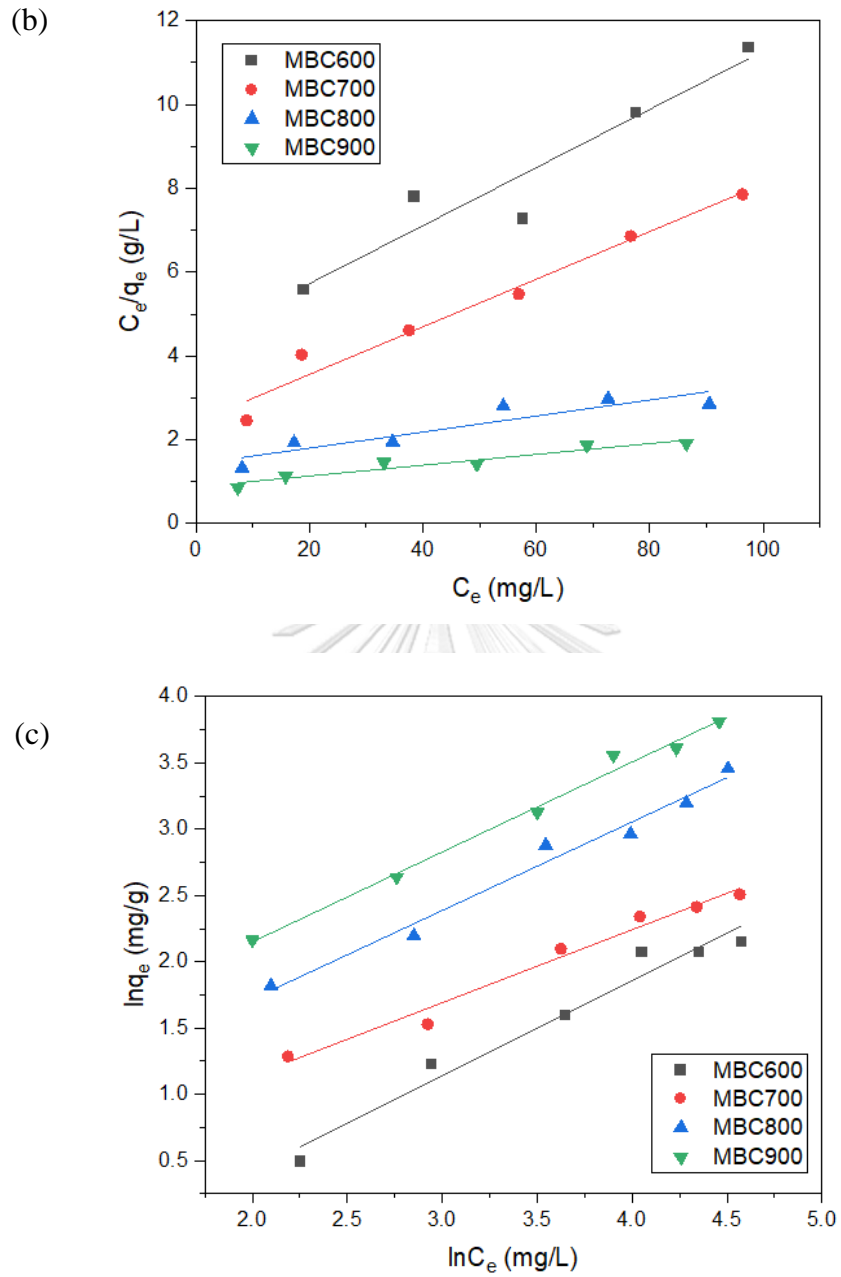


Fig. 4.10 (a) Adsorption isotherm, (b) Linearized Langmuir isotherm model, and (c) Linearized Freundlich isotherm model

Table 4.5 Adsorption isotherm parameter

Sample	Langmuir			Freundlich		
	q_m (mg/g)	K_L (L/mg)	R^2	N	K_F	R^2
MBC600	14.42	0.016	0.91	1.40	0.36	0.96
MBC700	17.59	0.023	0.97	1.82	1.04	0.98
MBC800	52.25	0.013	0.84	1.49	1.46	0.98
MBC900	77.60	0.014	0.92	1.47	2.21	0.99

By analyzing the effect of pyrolysis temperature on characteristics of MBC, MBC900 is found to possess the highest S_{BET} , V_P , I_G/I_D ratio, and M_S value. Moreover, the study of adsorption kinetics and isotherm experiments revealed that MBC900 possessed the highest maximum adsorption capacity. Therefore, MBC900 was selected for further investigation of TC antibiotic removal.

4.2.4 Effect of initial pH

The TC adsorption capacity of MBC900 under various initial pH is shown in **Fig. 4.10**. The surface charges of TC could be varied by changing the solution pH [23]. Therefore, electrostatic interaction could affect the adsorption mechanism. TC is amphoteric molecule with different charge under different pH (H_4TC^+ , pH < 3.3; H_3TC , pH = 3.3–7.7; H_2TC^- , pH = 7.7–9.7; HTC^{2-} , pH > 9.7)[86]. FTIR results confirmed that MBC possessed oxygenated group on its surface, which is negative charge. The adsorption capacity was highest at pH 3. At pH 3, TC was positive charge while MBC contain negative charge from oxygenated group. Therefore, electrostatic attraction occurred (i.e., positive-negative attraction). The adsorption capacity rapidly decreased from 21.67 to 8.31 mg/g when initial pH increased from 5 to 11. At pH 7, 25% of TC was anionic form[87] and at pH higher than 7, TC charge was more negative leading to an increase in electrostatic repulsion between TC molecule and MBC resulting in a decrease in adsorption capacity.

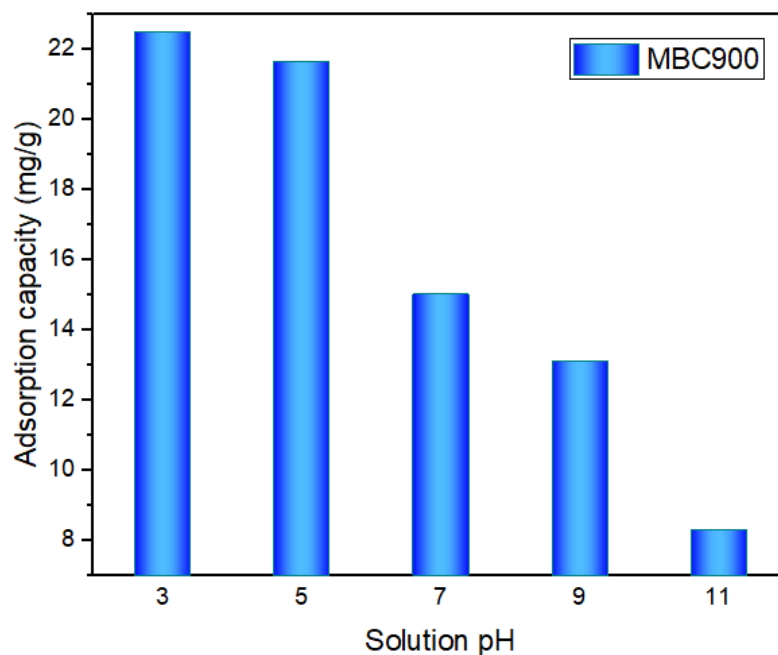


Fig. 4.11 Effect of initial pH on TC adsorption capacity

4.2.5 Reusability of MBC

The reusability test was performed by adsorption-desorption process in five cycles to study the stability of MBC900 as shown in **Fig. 4.11**. Percent of adsorption of each cycle was calculated by equation below:

$$\text{Adsorption percentage} = \frac{q_i}{q_1} \times 100 \quad (5)$$

Where q_i is adsorption capacity of cycle i and q_1 is adsorption capacity of first cycle.

Adsorption capacity decreased by less than 10% after three cycles (100 to 93.46%). After four cycles, adsorption capacity decreased by 10% (100 to 89.56%). The adsorption capacity decreased by 16% (100 to 83.89%) after five cycles, the decrease in adsorption capacity was due to the decrease in active sites of MBC after each regeneration cycle confirmed by S_{BET} of MBC before adsorption and after five cycles decreased from 401.11 m^2/g to 365.26 m^2/g . These results indicated that MBC was reusable and had good stability.

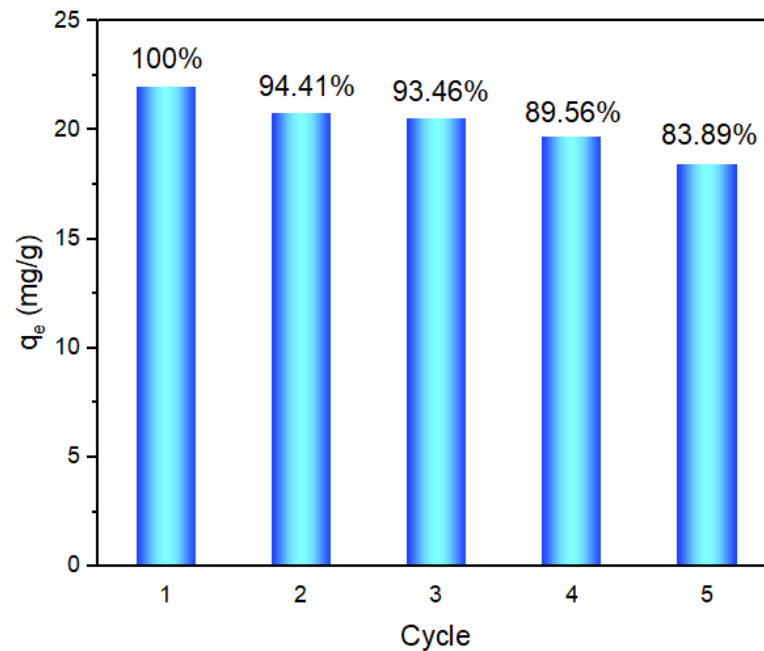


Fig. 4.12 Reusability of MBC900

4.3 Development of an empirical model of TC adsorption capacity

4.3.1 Development of an empirical model of TC adsorption capacity based on RSM

The development of an empirical model of TC adsorption capacity under four studied factors, including A-Initial TC concentration, B-Adsorbent dosage, C-Solution pH, and D-Contact time, which were experimentally studied following **Table 3.4**. The experimental adsorption capacities of each condition are shown in **Table 4.6**. The highest adsorption capacity of 69.61 mg/g could be obtained from Run number 15 (Initial concentration of 60 mg/L, adsorbent dosage of 0.3 mg/L, solution pH of 3, and contact time of 45 min).

An empirical model was generated by fitting it with quadratic model, which is exhibited in equation (3). Predicted adsorption capacities of each condition, which are calculated from equation (3) and exhibited in **Table 4.6**.

$$\begin{aligned} \text{Predicted adsorption capacity (mg/g)} = & -1.2+2.082A-40B-1.46C+0.213D- \\ & 0.00654A^2+14B^2+0.312C^2+0.00486D^2+0.352AB-0.169AC-0.0018AD+4.48BC- \\ & 0.198BD-0.0635CD \end{aligned} \quad (6)$$

Table 4.6 Experimental and predicted adsorption capacity under CCD design

Run	Initial TC concentration (mg/L)	Adsorbent dosage (g/L)	Solution pH	Time (min)	Experimental adsorption capacity (mg/g)	Predicted adsorption capacity (mg/g)
1	60	0.3	7	45	32.74	31.16
2	60	0.3	11	45	4.54	1.17
3	80	0.2	5	60	58.92	59.29
4	40	0.2	9	60	17.54	15.64
5	80	0.2	9	30	3.70	8.32
6	40	0.2	5	60	46.32	42.70
7	60	0.3	7	45	31.76	31.16
8	20	0.3	7	45	13.65	15.14
9	80	0.4	9	30	13.95	14.51
10	40	0.4	9	30	15.35	19.99
11	40	0.2	9	30	17.73	16.62
12	60	0.3	7	45	30.19	31.16
13	80	0.4	5	60	62.66	60.70
14	60	0.3	7	75	33.33	36.69
15	60	0.3	3	45	69.61	71.13
16	80	0.4	5	30	50.51	57.41
17	40	0.4	5	30	39.60	35.85
18	40	0.4	5	60	40.93	41.30
19	40	0.4	9	60	17.51	17.82
20	100	0.3	7	45	29.58	26.25
21	60	0.3	7	45	25.58	31.16
22	80	0.2	9	60	4.49	5.18
23	60	0.3	7	45	24.93	31.16
24	60	0.1	7	45	28.19	29.33
25	60	0.3	7	45	43.63	31.16
26	60	0.3	7	45	29.19	31.16
27	40	0.2	5	30	32.01	36.06
28	80	0.4	9	60	9.23	10.18
29	60	0.5	7	45	37.09	34.11
30	60	0.3	7	15	39.59	34.38
31	80	0.2	5	30	58.18	54.81

The plot between predicted adsorption capacity versus experimental data as shown in **Fig 4.12** revealed that the data arrangement is in line with the perfect line (blue line ($y=x$)) with a high R^2 value of 0.9492, suggesting that the prediction data is consistent with experimental data. Moreover, predicted R^2 of 0.8195 reasonable agreement with adjusted R^2 of 0.9048 because the difference was less than 0.2.

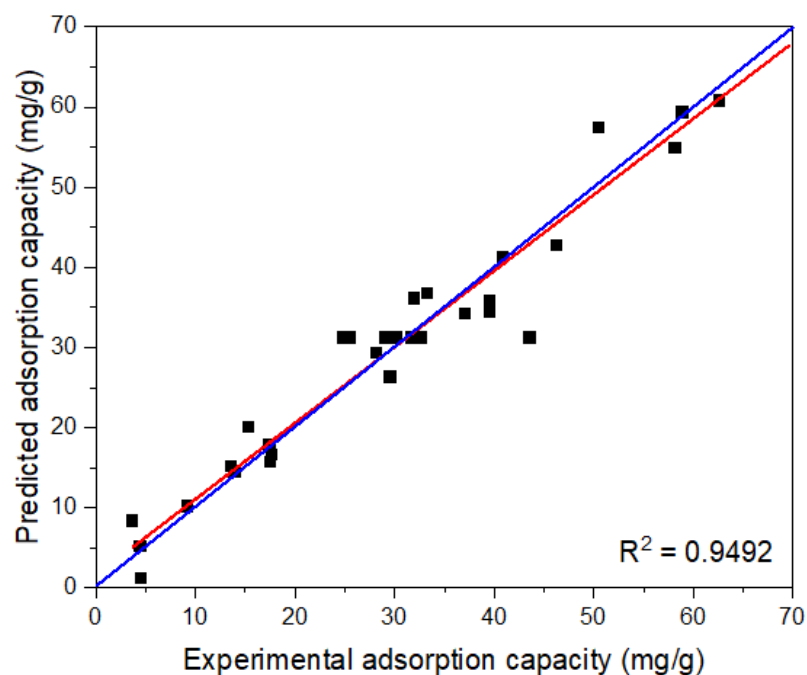


Fig. 4.13 Predicted adsorption capacity against experimental data (red line is regression line and blue line is perfect line ($y=x$))

The ANOVA results of empirical model of tetracycline adsorption capacity are exhibited in **Table 4.7**. At 95% confidence or level of significance equal to 0.05, when p-value less than 0.05 indicates model term is significant while p-value greater than 0.05 indicates model term is not significant. The model is significant with F-value of 21.37 and p-value less than 0.0001 while the lack of fit is not significant with F-value of 0.6 and p-value of 0.776. The significant effects of this model terms on TC adsorption capacity are initial TC concentration, solution pH, interaction between initial TC concentration and solution pH, and square effect of initial TC concentration with p-value less than 0.05. From sum of squares, the significant effect on TC

adsorption capacity is as follows order: solution pH > interaction between initial TC concentration and solution pH > square effect of initial TC concentration > initial TC concentration as shown in **Fig. 4.13**.

Table 4.7 ANOVA of an empirical model of tetracycline adsorption capacity

Source	Sum of squares	DF	Mean square	F-value	p-value
Model	8693.08	14	620.93	21.37	< 0.0001
A-Initial TC concentration	184.37	1	184.37	6.34	0.023
B-Adsorbent dosage	34.22	1	34.22	1.18	0.294
C-Solution pH	7342.3	1	7342.3	252.67	< 0.0001
D-Time	8.24	1	8.24	0.28	0.6022
A ²	195.86	1	195.86	6.74	0.019
B ²	0.55	1	0.55	0.02	0.892
C ²	44.53	1	44.53	1.53	0.234
D ²	34.23	1	34.23	1.18	0.294
AB	7.92	1	7.92	0.27	0.609
AC	731.16	1	731.16	25.16	< 0.0001
AD	4.69	1	4.69	0.16	0.693
BC	12.82	1	12.82	0.44	0.516
BD	1.4	1	1.4	0.05	0.829
CD	58.06	1	58.06	2.00	0.177
Error	464.94	16	29.06		
Lack-of-Fit	231.82	10	23.18	0.6	0.776
Pure Error	233.11	6	38.85		
Total	9158.02	30			

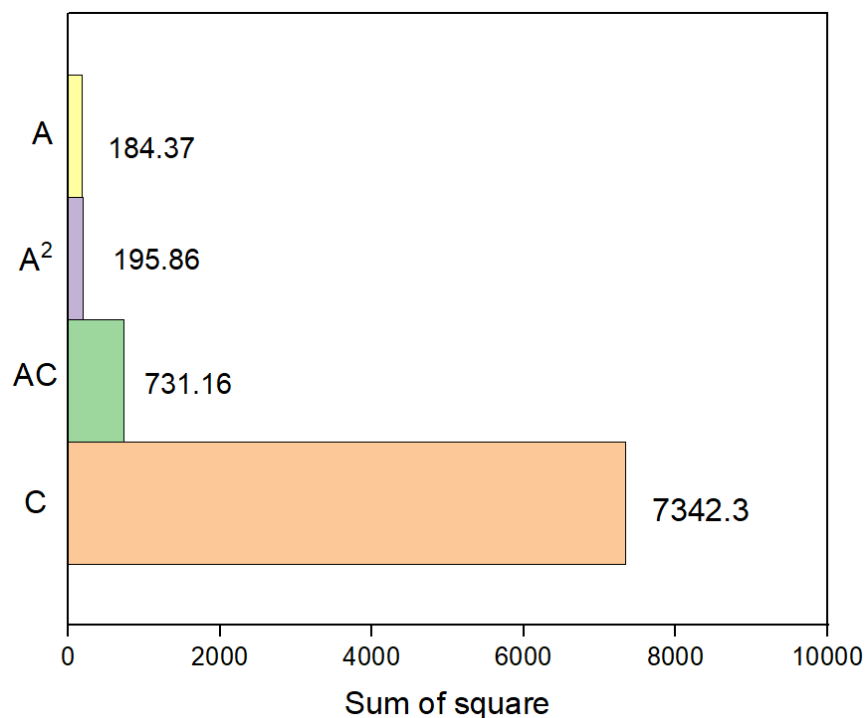
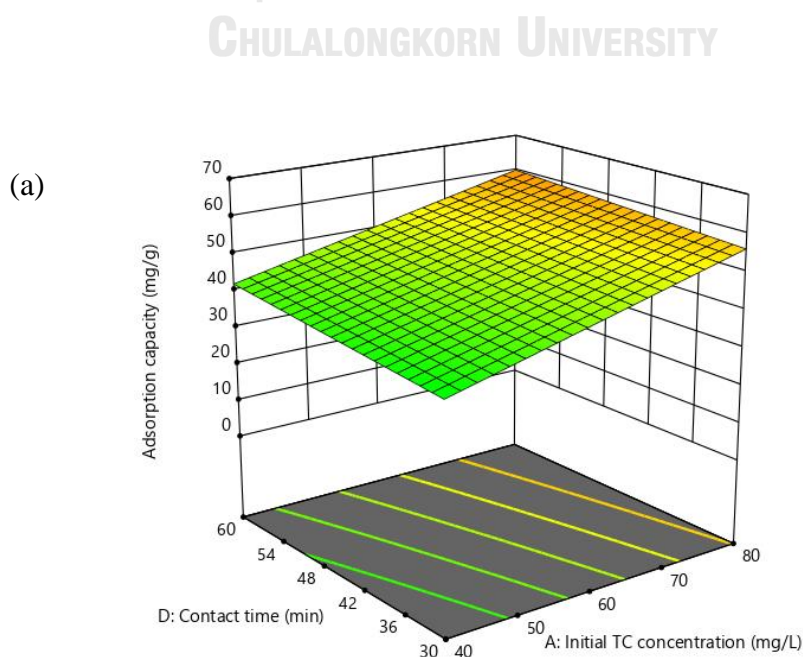


Fig. 4.14 Sum of squares of significantly terms

3-D Plots of interaction effect are exhibited in **Fig. 4.14(a-c)**, which could provide a clear understanding of how these factors interacted and gave synergistic effects on the sorption capacity. There are three interaction effects discussed in this section, including initial TC concentration-contact time, solution pH-adsorbent dosage, and initial TC concentration-solution pH. **Fig. 4.14a** shows the interaction effect between initial TC concentration and contact time on adsorption capacity. At each level of initial TC concentration in the range of 40-80 mg/L, contact times varied from 30 - 60 min do not affect adsorption capacity. From adsorption kinetics, the adsorption capacity slightly increases after 30 min and there are small differences in adsorption capacity between 30 to 60 min of contact time. Therefore, the effect of contact time in the range of 30 to 60 min could not affect the adsorption capacity. In the case of the effect of initial TC concentration, **Fig. 4.14a** reveals that, with an increase in initial TC concentration from 40 mg/L to 80 mg/L, adsorption capacity was increased. Because an increase in TC concentration leads to increase in driving force or concentration gradient, resulting in adsorption capacity increased.

The effect of interaction between solution pH and adsorbent dosage on adsorption capacity is shown in **Fig. 4.14b**. At each level of solution pH, the adsorbent dosages varied from 0.2-0.4 g/L do not affect the adsorption capacity due to the adsorption capacity was calculated by the amount of adsorbed TC per mass of the adsorbent [88]. However, the adsorbent dosage affects adsorption efficiency with the result provided in **Fig. 1A**. **Fig. 4.14b** also shows effect of solution pH while constant adsorbent dosage. The highest adsorption capacity could be obtained at low pH. When solution pH was increased, adsorption capacity decreased. The result is consistent with **Fig.4.10**. Because of the effect of electrostatic attraction between TC which is positive charge and MBC which is negative charge from oxygen group at high pH. Meanwhile, electrostatic repulsion between TC and MBC are both negative charges at low pH.

Fig. 4.14c shows the decrease in adsorption capacity at high initial TC concentration and high solution pH with constant adsorbent dosage. This is because, at high pH, an increase of Na^+ from NaOH solution that can be competitive to TC molecules [89] indicates at a high concentration of TC, there is not enough site available for TC molecules. These results are also consistent with a previous study by M. Foroughi et al. [63]. With the increase in initial TC concentration at low solution pH, the adsorption capacity was increased. Because of an increase in concentration gradient which has been explained in the above paragraph.



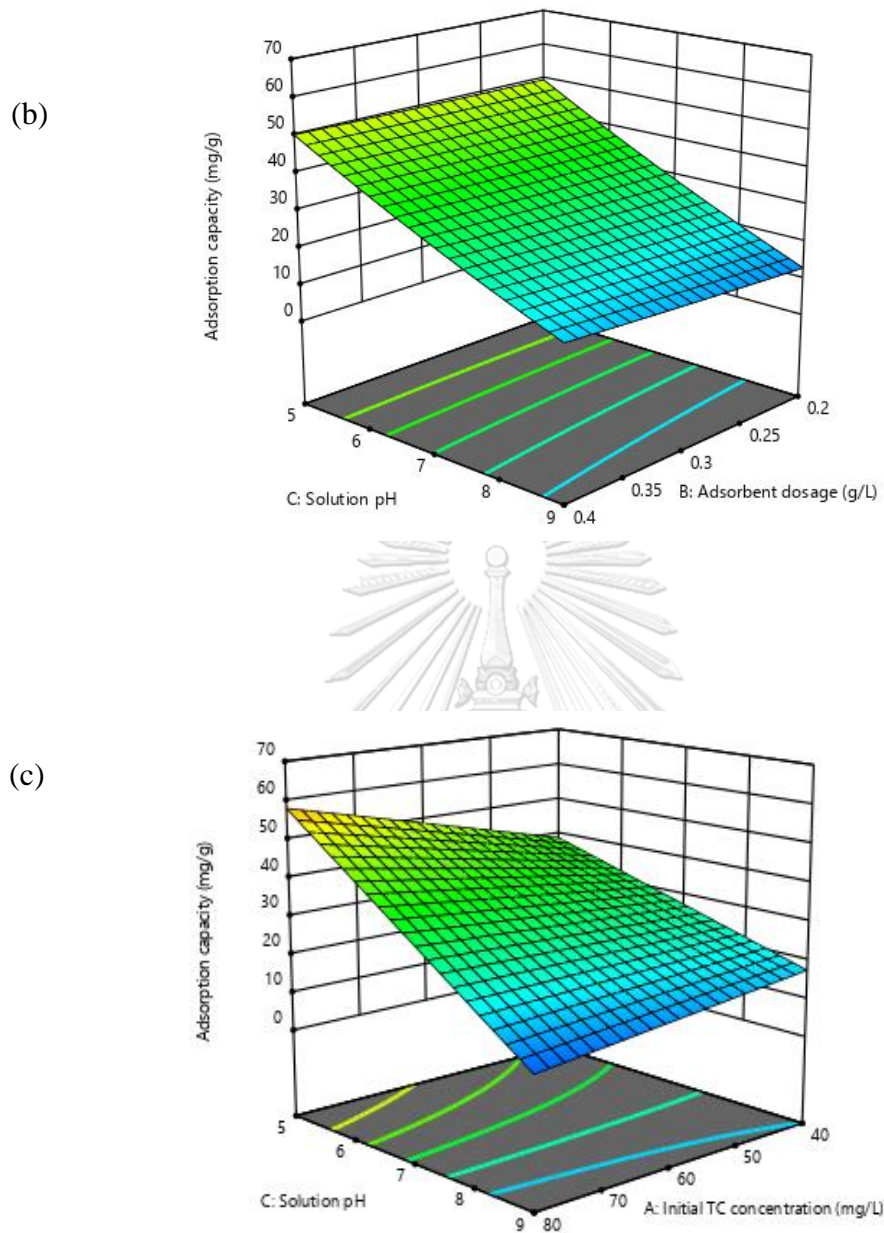


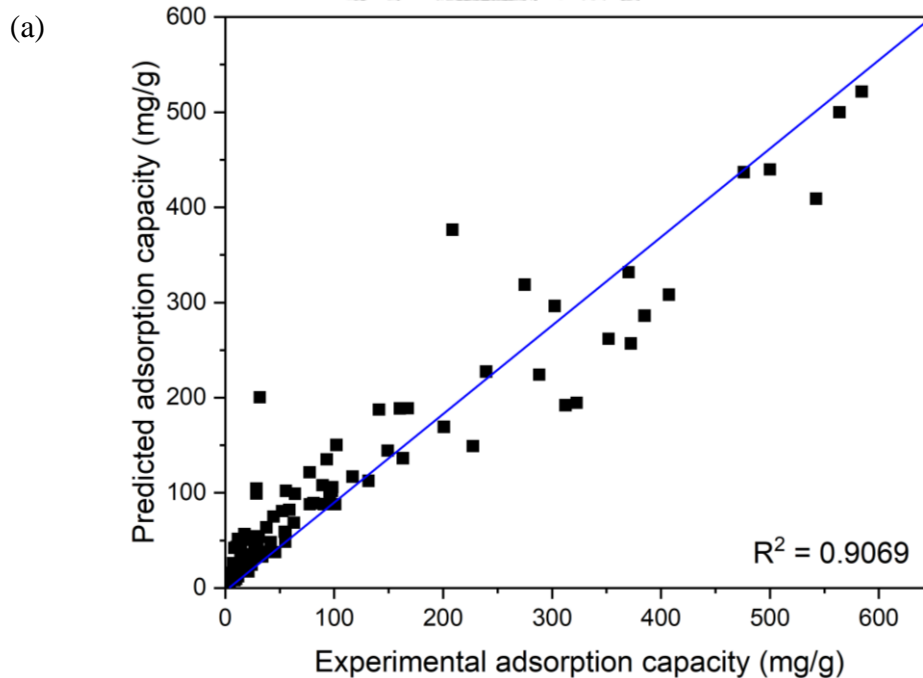
Fig. 4.15 3-D surface plots of an interaction effect between (a) Initial TC concentration and contact time (b) Solution pH and adsorbent dosage (c) Initial TC concentration and solution pH on adsorption capacity

4.3.2 Development of semi-empirical model of TC adsorption capacity based on ML

The collected data of training data set were used to develop the model for prediction of TC adsorption capacity under influential factors including S_{BET} ,

(O+N)/C, H/C, C%, and initial TC concentration. The plots of predicted adsorption capacity versus experimental adsorption capacity from random forest, Catboost, and boosted regression tree algorithms are shown in **Fig. 4.16-18**, respectively. The results revealed that Catboost provides the highest R^2 followed by random forest and boosted regression tree.

The testing data, which are considered as new observation data, were used to validate the models. The result is in the term of predicted R^2 . The highest predicted R^2 could be obtained in Catboost of 0.7426, while predicted R^2 of random forest and boosted regression tree are 0.6419 and 0.5671, respectively. The novelty of machine learning models is that they could develop the model using the data from literature. Moreover, the fundamental assumptions of traditional isotherm models are not needed. Therefore, the use of machine learning models are better in applications and different types of adsorbents[23].



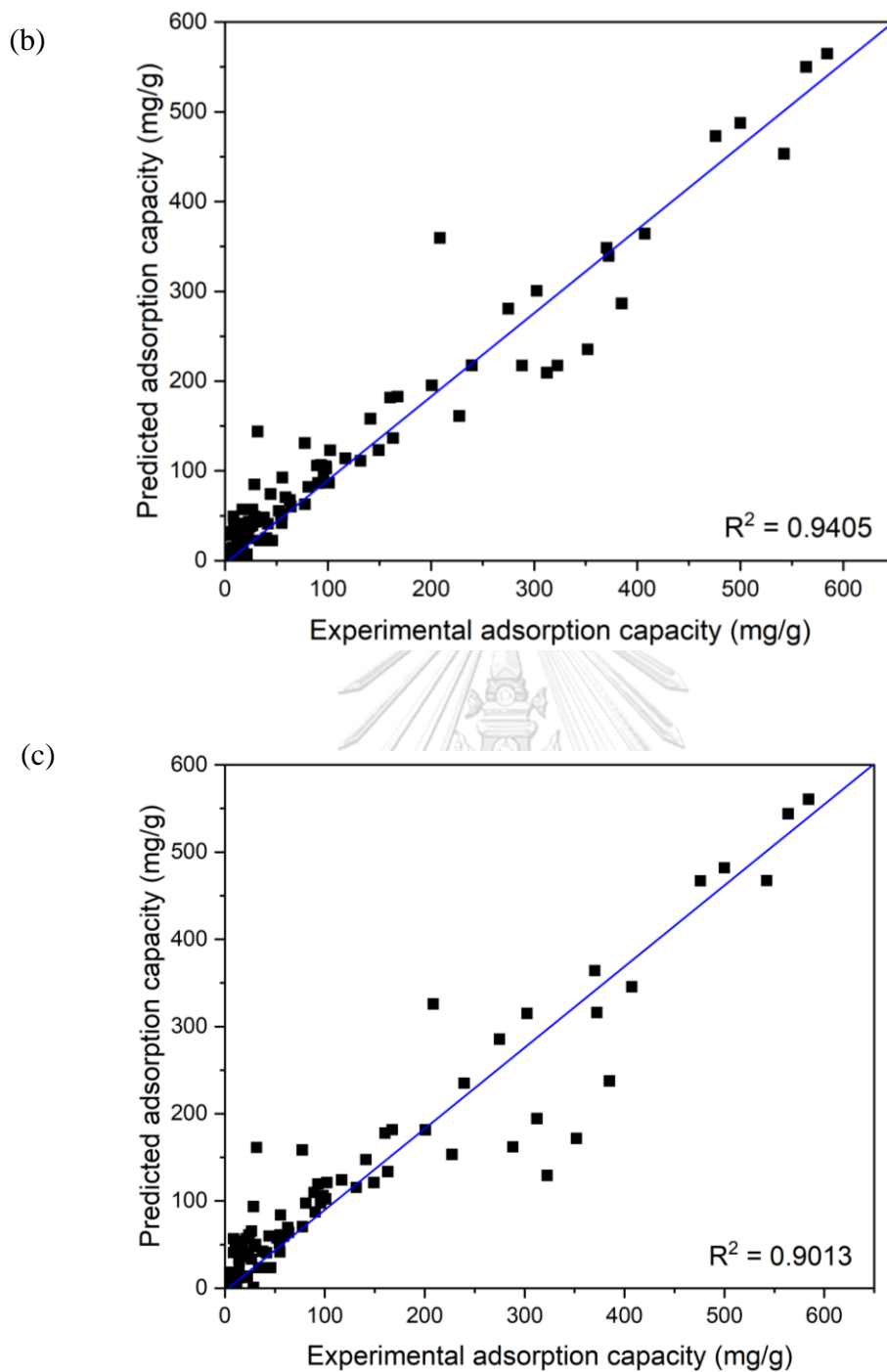


Fig. 4.16 Predicted adsorption capacity versus experimental adsorption capacity from (a) random forest, (b) Catboost, and (c) boosted regression tree algorithms

The highest R^2 and predicted R^2 could be obtained from Catboost model. Thus, a feature of importance is performed based on Catboost algorithms. The factor

with a larger effect on TC adsorption capacity possesses a higher score of feature importance as shown in **Fig. 4.18**. The order of feature importance is $S_{\text{BET}} > (\text{O+N})/\text{C} > \text{initial TC concentration} > \text{H/C} > \text{C\%}$. The higher S_{BET} could provide a more active site for binding TC molecules. $(\text{O+N})/\text{C}$ represents the hydrophobicity of adsorbents. There is hydrophobic interaction between TC and adsorbent [90]. With the decrease in $(\text{O+N})/\text{C}$ of the adsorbents, hydrophobicity increased. Therefore, it would enhance hydrophobic interaction. Initial TC concentration affects adsorption capacity by increasing the driving force. H/C ratio indicates the degree of aromaticity of adsorbents, which could act as electron acceptors. There is aromatic ring structure in TC molecule, which could act as electron donor. Therefore, H/C ratio could affect to π - π electron donor-acceptor (EDA) interactions between adsorbent and TC molecules[4].

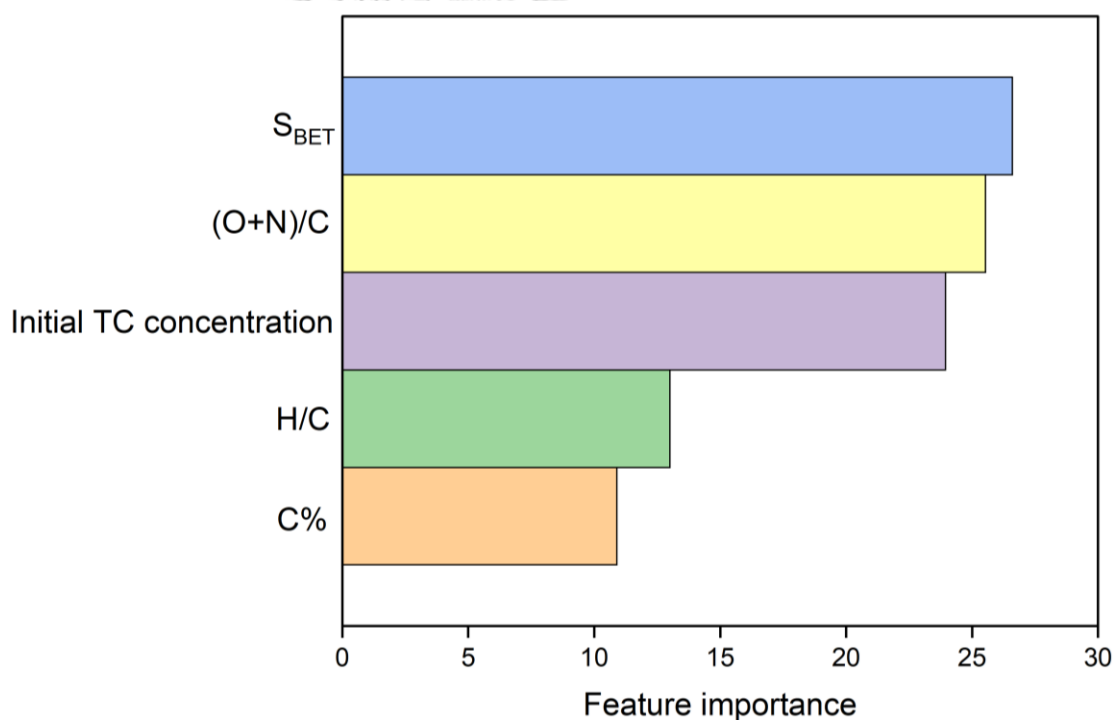


Fig. 4.17 Feature importance of influential factors on TC adsorption capacity

CHAPTER 5

CONCLUSIONS AND RECOMMENDATIONS

This chapter provided conclusions of key findings in this work. This work included three main investigations: (i) the study of effect of pyrolysis temperature on characteristics of magnetic biochar (ii) the study of TC adsorption experiments including adsorption kinetics, adsorption isotherm, effect of solution pH, and reusability of MBC (iii) the study of development of an empirical model of TC adsorption capacity under various adsorption conditions using RSM. Lastly, this chapter provided some recommendations from this research work for guidance a future investigation.

5.1 Conclusions

5.1.1 Effect of pyrolysis temperature on characteristics of magnetic biochar

Magnetic biochar (MBC) has been widely employed in environmental remediation, especially in adsorption of contaminants. MBC has been employed as the adsorbent for adsorption process due to the facile separation of MBC after treatment process via utilizing its magnetic properties. There are various methods for synthesis of MBC such as impregnation-pyrolysis, chemical co-precipitation, solvothermal, and reductive co-precipitation. In this work, impregnation pyrolysis was selected due to its advantage in time-saving and good stability of product could be obtained. Abundant available agricultural waste which is watermelon rind impregnated with FeCl_3 as famous magnetic precursor was used to produce MBC. One important factor for synthesis of MBC such as pyrolysis temperature was investigated. The effect of pyrolysis temperature was studied at 600, 700, 800, and 900 °C. For the synthesis, watermelon rind was impregnated with FeCl_3 . Impregnated watermelon rind was put in ceramic boat, then, placed in quartz tube in electrical furnace. The temperature was increased with a constant heating rate until reached a setting point (600, 700, 800, and 900 °C) and held for 2 hr, then cooling

down to room temperature. After cooling down, MBC product was collected and weighted for determining the product yield.

It was found that product yield dramatically decreased with an increase in pyrolysis temperature. Because the increase in pyrolysis temperature could enhance the decomposition of lignocellulose and volatile components. In addition, various characterization techniques including SEM, N₂ adsorption/desorption, elemental analyzer, FTIR, Raman, XRD, and VSM were applied to study properties of MBC such as morphology, specific surface area, chemical composition, surface functional group, crystallinity, magnetic phase, and magnetic property. It was found that pyrolysis temperature exhibits a significant effect on properties of MBC samples, for example, specific surface area and graphitic carbon would enhance by increasing pyrolysis temperatures. Additionally, magnetic phase was reduced from Fe₃O₄ to Fe with higher *M_s* values and lower *H_c* values when pyrolysis temperature increased from 600 °C to 900 °C.

5.1.2 Adsorption of tetracycline

MBC samples were employed as adsorbents for studying adsorption of tetracycline (TC). Adsorption kinetics and isotherm experiment were conducted to study adsorption behaviors. Effects of solution pH and reusability were also examined.

5.1.2.1 Adsorption kinetics

The study of adsorption kinetic was experimentally conducted using 40 mg/L and 50 mL of TC with adding 15 mg of MBC. The solution was periodically taken off for TC concentration measurement between 5-180 min. It was found that the adsorption process reached equilibrium within 60 min. In addition, the adsorption process of MBC600 followed pseudo-first-order kinetic model while MBC700, MBC800, and MBC900 followed pseudo-second-order kinetic model.

5.1.2.2 Adsorption isotherm

Langmuir and Freundlich's models were applied to study adsorption isotherm of TC adsorption. The experiments were conducted by varying initial TC

concentrations in the range of 10 – 100 mg/L with 50 mL of TC, then adding 15 mg of MBC. The result revealed that all MBC samples fitted with Freundlich isotherm model better than Langmuir isotherm model suggesting the adsorption process is based on heterogeneous adsorption site.

5.1.2.3 Effect of solution pH

Effect of solution pH on TC adsorption capacity of MBC was studied. The solution pH was studied in the range of 3-11. The solution pH was adjusted by HCl and NaOH solution. It was found that the adsorption process was pH-dependent due to effect of electrostatic force between TC and MBC. The electrostatic attraction between TC molecule which is positive charge and MBC which is negative charge from oxygenated group. Meanwhile, the electrostatic repulsion between TC molecule and MBC are both negative charges. Therefore, the adsorption capacity of 22.51 mg/g could be obtained at pH 3 when pH was increased to pH 11, the adsorption capacity decreased to 8.31 mg/g.

5.1.2.4 Reusability test

The ideal adsorbent is the adsorbent with easy separation from the solution and excellent reusability. In this work, MBC could easily separate from TC solution via inducing by the external magnet. Moreover, the reusability test confirmed that MBC provides good recyclability and reusability with adsorption capacity of 83.89% (compared with the first cycle) after five cycles.

5.1.3 Development of an empirical model

Adsorption conditions and characteristics of adsorbent are the main influential factors on TC adsorption capacity. In this work, response surface methodology (RSM) and machine learning (ML) were applied to develop the empirical model and semi-empirical models.

5.1.3.1 Development of empirical model based on RSM

The adsorption conditions are one of influential factors, which are affecting the adsorption capacity of MBC toward TC. Central composite design (CCD) was applied to design the experimental runs under studied factors such as initial TC

concentration, adsorbent dosage, solution pH, and contact time. In the studied range of 20-100 mg/g of initial TC concentration, 0.1-0.5 g/L of adsorbent dosage, 3-11 of solution pH, and 15-75 min of contact time. The results were analyzed by RSM. From ANOVA results at 95% confidence, the model is significant with high R^2 of 0.9492. The order of influential terms is solution pH > interaction between initial TC concentration and solution pH > square effect of initial TC concentration > initial TC concentration.

5.1.3.2 Development of semi-empirical model based on ML

Apart from the adsorption conditions, characteristics of the adsorbent such as S_{BET} , (O+N)/C, H/C, C%, and initial TC concentration are influential factors affecting the TC adsorption capacity. Three different ML algorithms including random forest (RF), Catboost, and boosted regression tree (BRT) were used to develop the semi-empirical model by using 96 data from literature and 4 data from this work. It was found that Catboost outperformed random forest and boosted regression tree. The feature important revealed S_{BET} provided the largest effect on TC adsorption capacity followed by (O+N)/C, initial TC concentration, H/C, and C%.

5.2 Recommendations for future work

This work studied only preliminary effect of impregnation ratio between watermelon rind and $FeCl_3$ on tetracycline adsorption capacity. There is no characterization of synthesized magnetic biochar from different impregnation ratios. Therefore, the effect of impregnation ratio between watermelon rind and $FeCl_3$ should be more studied. In addition, the study of feature importance cannot tell whether it had positive or negative effect on TC adsorption capacity. Thus, the effect of each influential factor should be studied in the future. Moreover, if the data were more collected from literature, it can improve the accuracy of the development model.

APPENDIX A

Preparation of watermelon rind impregnated with FeCl₃

FeCl₃.6H₂O was used as magnetic precursor to impregnate with watermelon rind. Impregnation ratio between watermelon rind and FeCl₃ of 2:1 was used for the whole investigation. The calculation of FeCl₃.6H₂O requirement was shown in Equation A.1

$$\text{FeCl}_3 \cdot 6\text{H}_2\text{O required per 1 g of watermelon rind} = \frac{MW_{\text{Iron chloride hexahydrate}} \times 2}{MW_{\text{Iron chloride}}} \quad (\text{A.1})$$

Where,

MW_{Iron chloride hexahydrate} is molecular weight of FeCl₃.6H₂O (270 g/mol)

MW_{Iron chloride} is molecular weight of FeCl₃. (162 g/mol)

Example

$$\text{FeCl}_3 \cdot 6\text{H}_2\text{O required per 1 g of watermelon rind} = \frac{270 \times 2}{162} = 3.33 \text{ g}$$

APPENDIX B

Size analysis of magnetic particle

The size of magnetic particle was analyzed to study characteristics of magnetic property. In this case, MBC900 was used to analyze because there is only α -Fe on its surface. The diameter of α -Fe was analyzed using SEM image of MBC900 at 1300X magnification as shown in **Fig. B1** with Image processing and Analysis in Java (ImageJ). Fifty of α -Fe (spherical particles) were selected to analyze the diameter ($N = 50$) with the data shown in **Table B.1**.

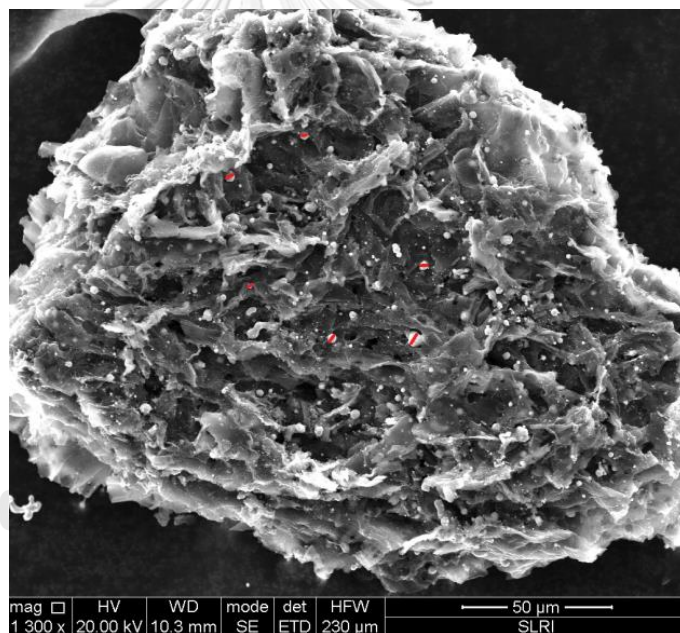


Fig. B1 SEM image of MBC900 (red line shows how to collect the data for ImageJ)

Table B.1 Diameter analysis data of α -Fe

Label	Diameter (μm)
1	2.07
2	1.92
3	1.85
4	1.93
5	1.79
6	1.63
7	1.81
8	2.07
9	1.35
10	1.50
11	2.07
12	2.02
13	4.04
14	1.81
15	1.63
16	0.92
17	2.34
18	1.81
19	2.70
20	2.01
21	1.00
22	2.70
23	3.05
24	2.12
25	2.85
26	2.70
27	2.62
28	2.29
29	1.36
30	1.36
31	1.92
32	1.79
33	2.48
34	1.79
35	2.34
36	3.27
37	1.79
38	1.42

39	2.62
40	2.69
41	1.92
42	2.73
43	1.85
44	2.01
45	2.01
46	2.07
47	2.02
48	1.50
49	1.81
50	2.25
Mean	2.07
Standard deviation	0.57



APPENDIX C

Product yield of synthesized MBC

Weight of watermelon rind impregnated with FeCl₃ and weight of product at various pyrolysis temperatures are shown in **Table C.1** while product yield of synthesized MBC at various pyrolysis temperatures was calculated by Equation C.1. and was shown in **Table C.2**.

Table C.1 Weight of watermelon rind impregnated with FeCl₃ and weight of product at various pyrolysis temperatures

Sample	Repeatability	Weight of watermelon rind impregnated with FeCl ₃ (g)	Weight of product (g)
MBC600	Run 1	2.0045	0.6906
	Run 2	2.0078	0.6798
	Run 3	2.0061	0.6466
MBC700	Run 1	2.0014	0.6290
	Run 2	2.0070	0.6200
	Run 3	2.0056	0.6109
MBC800	Run 1	2.0034	0.5814
	Run 2	2.0074	0.5866
	Run 3	2.0055	0.5347
MBC900	Run 1	2.0047	0.5645
	Run 2	2.0088	0.5024
	Run 3	2.0048	0.5437

$$\text{Product yield (\%)} = \frac{W_p}{W_{WIF}} \times 100\% \quad (\text{C.1})$$

Where,

W_p is weight of product

W_{WIF} is weight of watermelon rind impregnated with FeCl₃

Example

$$\text{Product yield (\%)} = \frac{0.6906}{2.0045} \times 100\% = 34.45 \%$$

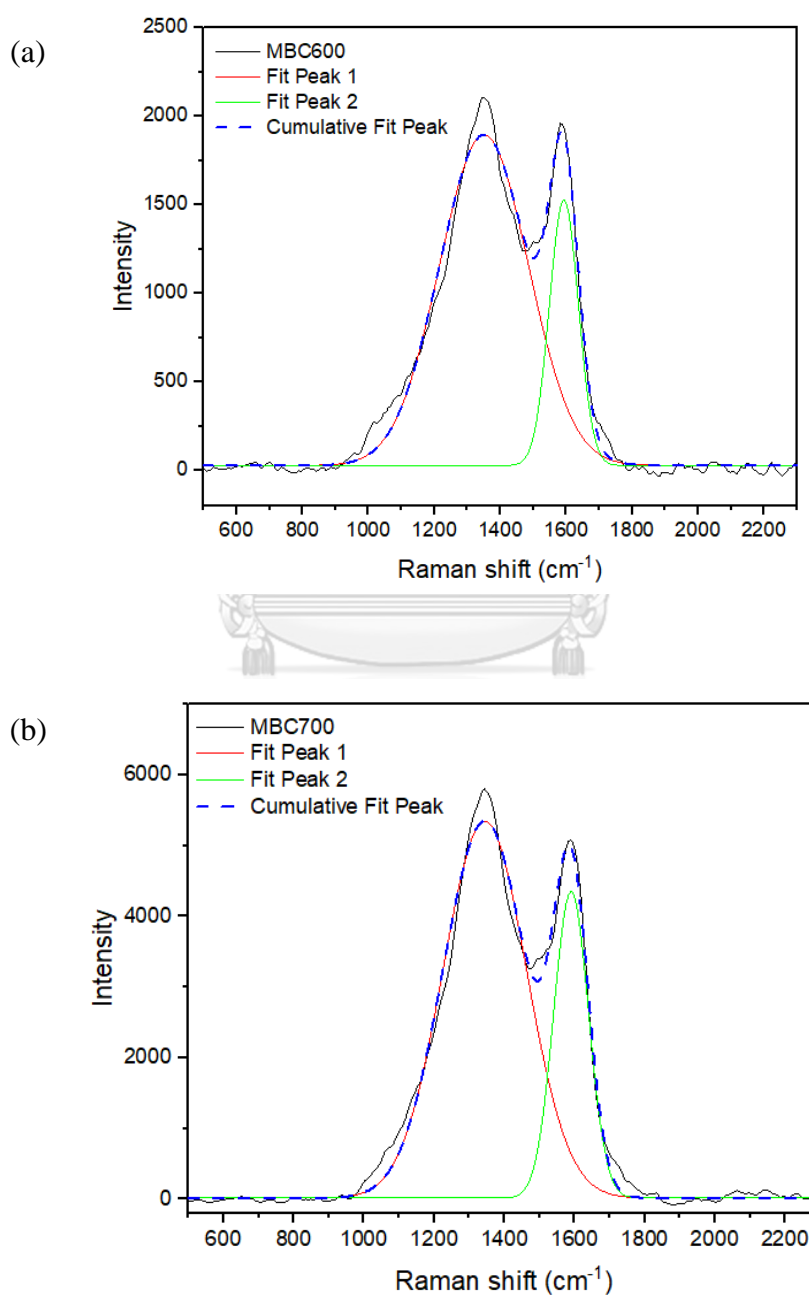
Table C.2 Product yield (%) of synthesized MBC at various pyrolysis temperatures

Sample	Repeatability	Yield (%)	Average yield (%)	Standard deviation
MBC600	Run 1	34.45	33.51	0.94
	Run 2	33.86		
	Run 3	32.23		
MBC700	Run 1	31.43	30.93	0.40
	Run 2	30.89		
	Run 3	30.46		
MBC800	Run 1	29.02	28.30	1.16
	Run 2	29.22		
	Run 3	26.66		
MBC900	Run 1	28.16	26.76	1.31
	Run 2	25.01		
	Run 3	27.12		

APPENDIX D

Curve fitting of Raman spectra

The Raman spectra of all synthesized MBC were fitted by Origin 2021 to find the intensity of D-band and G-band as shown in **Fig. E1 (a-d)**. The obtained data were used to calculate the I_G/I_D ratio.



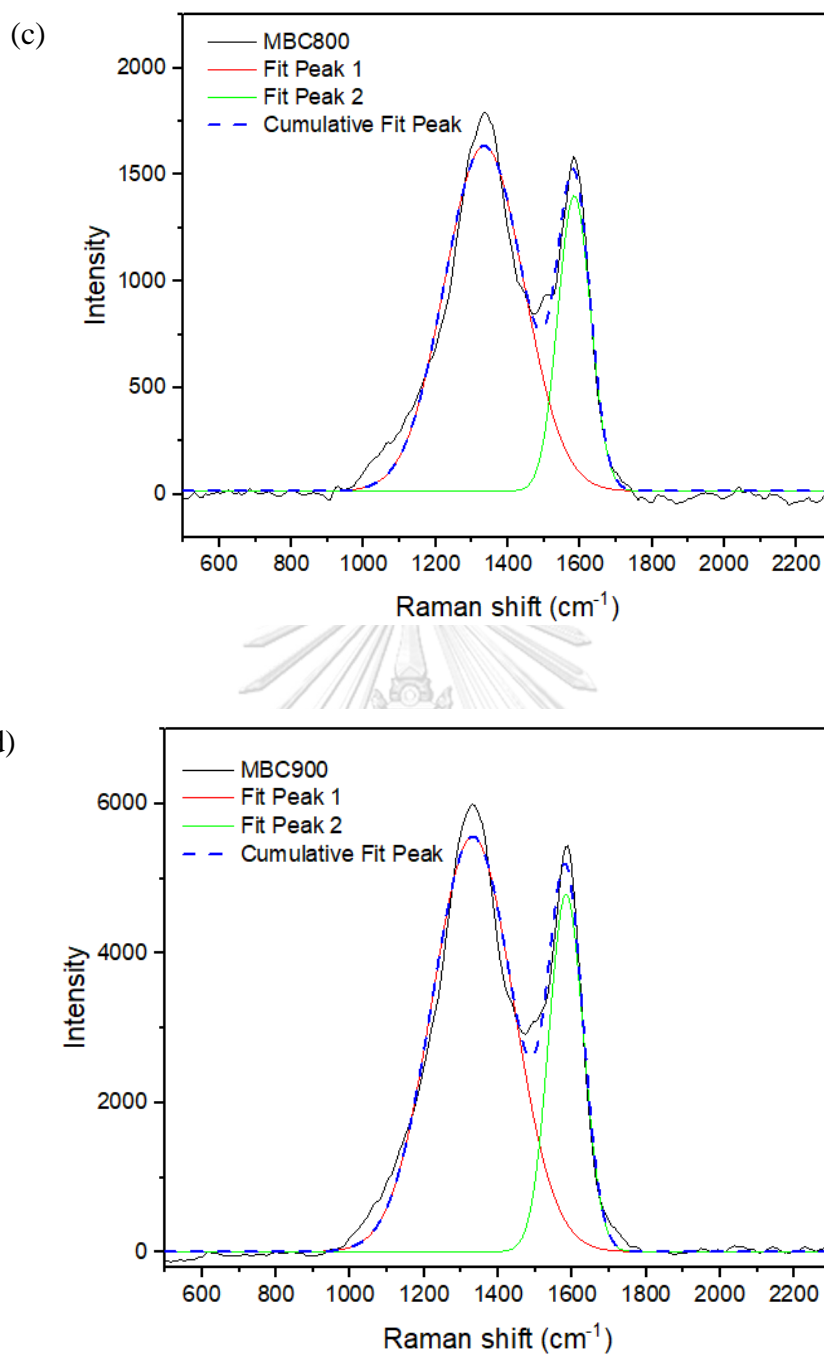


Fig. D1 Raman spectra of synthesized MBC at various pyrolysis temperatures (a) 600 °C (b) 700 °C (c) 800 °C and (d) 900 °C

APPENDIX E

Adsorption of TC

The experimental results of TC adsorption kinetics and isotherm are shown in **Table E.1** and **Table E.2**. Meanwhile, linearized fitting of each equation is also provided in this part.

Table E.1 Experimental data of TC adsorption capacity of MBCs at different contact times

Time (t) (s)	Adsorption capacity (q_t) (mg/g)			
	MBC600	MBC700	MBC800	MBC900
0	0.00	0.00	0.00	0.00
5	0.00	2.87	5.99	7.62
10	0.18	4.95	9.68	13.35
20	0.20	6.44	11.04	15.76
30	0.24	6.93	12.09	17.84
45	1.63	7.31	15.69	18.45
60	1.85	7.59	15.89	18.69
90	2.65	8.44	16.63	19.76
120	3.01	8.51	16.44	21.75
180	3.16	8.57	16.15	21.88

Linearized fitting of pseudo-first-order kinetics equation:

$$\text{MBC600 : } y = -0.011x + 1.495$$

$$\text{MBC700 : } y = -0.042x + 1.878$$

$$\text{MBC800 : } y = -0.056x + 2.742$$

$$\text{MBC900 : } y = -0.040x + 2.792$$

Linearized fitting of pseudo-second-order kinetics equation:

$$\text{MBC600 : } y = 0.207x + 17.629$$

$$\text{MBC700 : } y = 0.110x + 1.039$$

$$\text{MBC800} : y = 0.058x + 0.472$$

$$\text{MBC900} : y = -0.044x + 0.435$$

The kinetics constants such as rate constant (k) and equilibrium concentration were calculated using slope and intercept of linearized equation as below.

Example The calculation of pseudo-first-order kinetics parameter

$$\text{MBC700} : \text{Slope} = \frac{-k_1}{2.303}$$

$$-0.042 = \frac{-k_1}{2.303}$$

$$k_1 = 0.097 \text{ min}^{-1}$$

$$\text{Intercept} = \ln q_e$$

$$1.878 = \ln q_e$$

$$q_e = \exp(1.878)$$

$$q_e = 6.54 \text{ mg.g}^{-1}$$



Example The calculation of pseudo-second-order kinetics parameter

$$\text{MBC700} : \text{Slope} = \frac{1}{q_e}$$

$$0.110 = \frac{1}{q_e}$$

$$q_e = 9.09 \text{ mg.g}^{-1}$$

$$\text{Intercept} = \frac{1}{k_2 q_e^2}$$

$$1.039 = \frac{1}{k_2 \times 9.09^2}$$

$$k_2 = 0.012 \text{ g.mg}^{-1}\text{min}^{-1}$$

Table E. 2 Experimental data of TC adsorption isotherm with initial TC concentration varied from 10-100 mg/L

MBC600		MBC700		MBC800		MBC900	
C _e (mg/L)	q _e (mg/g)	C _e (mg/L)	q _e (mg/g)	C _e (mg/L)	q _e (mg/g)	C _e (mg/L)	q _e (mg/g)
9.51	1.63	8.91	3.62	8.15	6.16	7.39	8.70
18.98	3.40	18.61	4.61	17.30	8.98	15.81	13.98
38.52	4.94	37.56	8.14	34.66	17.79	33.17	22.77
57.62	7.92	56.88	10.39	54.19	19.36	49.50	34.98
77.62	7.92	76.65	11.17	72.67	24.45	68.91	36.95
97.43	8.58	96.32	12.27	90.50	31.68	86.44	45.21

Linearized Langmuir isotherm equation :

MBC600: $y = 0.069x + 4.338$

MBC700: $y = 0.057x + 2.422$

MBC800: $y = 0.019x + 1.419$

MBC900: $y = 0.013x + 0.877$

Linearized Freundlich isotherm equation :

MBC600: $y = 0.716x - 1.007$

MBC700: $y = 0.550x - 0.039$

MBC800: $y = 0.668x + 0.381$

MBC900: $y = 0.678x + 0.792$

The calculation of Langmuir and Freundlich isotherm parameter is calculated using slope and intercept of linearized equation as follows.

Example The calculation of Langmuir isotherm parameter:

$$\text{MBC700 : Slope} = \frac{1}{q_m}$$

$$0.057 = \frac{1}{q_m}$$

$$q_m = 17.54 \text{ mg.g}^{-1}$$

$$\text{Intercept} = \frac{1}{q_m \times K_L}$$

$$2.422 = \frac{1}{17.54 \times K_L}$$

$$K_L = 0.023 \text{ L.mg}^{-1}$$

Example The calculation of Freundlich isotherm parameter:

$$\text{MBC700: Slope} = \frac{1}{n}$$

$$0.550 = \frac{1}{n}$$

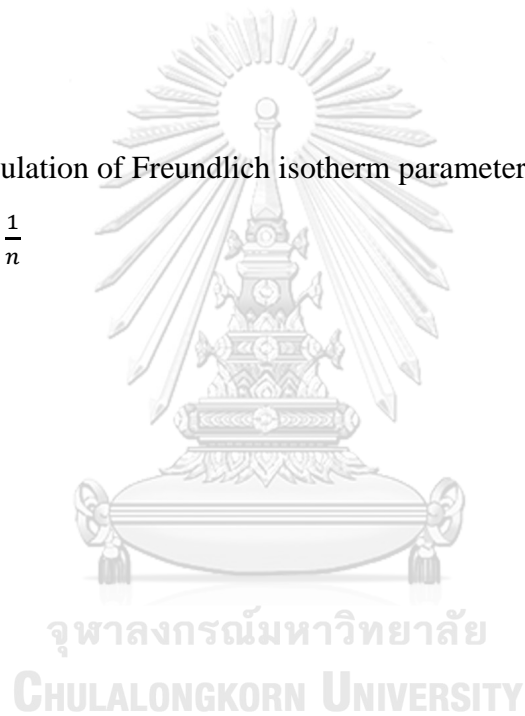
$$n = 1.182$$

$$\text{Intercept} = \ln K_F$$

$$-0.039 = \ln K_F$$

$$K_F = \exp(-0.039)$$

$$K_F = 1.04$$



APPENDIX F

Source code of ML

The source code of random forest algorithm is as follows.

```

# data analysis and wrangling
import pandas as pd
import numpy as np
import random as rnd

# visualization
import seaborn as sns
import matplotlib.pyplot as plt
from scipy.stats import norm
from scipy import stats
%matplotlib inline

# machine learning
from sklearn.linear_model import LinearRegression
from sklearn.ensemble import RandomForestRegressor
from sklearn.preprocessing import PolynomialFeatures
from sklearn.svm import SVR
from sklearn.ensemble import BaggingRegressor
from lightgbm import LGBMRegressor
from xgboost import XGBRegressor
from sklearn.ensemble import GradientBoostingRegressor
from sklearn.preprocessing import StandardScaler
from sklearn.metrics import mean_squared_error

```



จุฬาลงกรณ์มหาวิทยาลัย
CHULALONGKORN UNIVERSITY


```

from sklearn.metrics import r2_score

#K-Cross-Validation

from sklearn.model_selection import RepeatedStratifiedKFold
from sklearn.model_selection import GridSearchCV
from sklearn.model_selection import RepeatedKFold
from sklearn.model_selection import KFold, cross_val_score, train_test_split

dataset = pd.read_excel('Data-for-ML.xlsx')
dataset["Sbet"].fillna(dataset["Sbet"].mean(), inplace = True)
dataset["%C"].fillna(dataset["%C"].mean(), inplace = True)
dataset["H/C"].fillna(dataset["H/C"].mean(), inplace = True)
dataset["(O+N)/C"].fillna(dataset["(O+N)/C"].mean(), inplace = True)
X = dataset.iloc[:, 1:-1].values
y = dataset.iloc[:, -1].values

scalerX = StandardScaler()
scaledX = scalerX.fit_transform(X)
X = scaledX
scalerY = StandardScaler()
scaledY = scalerY.fit_transform(y.reshape(-1, 1))
y = scaledY.reshape(100)

from sklearn.model_selection import train_test_split
X_train, X_test, y_train, y_test = train_test_split(X, y, test_size = 0.15, random_state
= 1)

# define models and parameters
model = RandomForestRegressor()

```

```

n_estimators = [10 , 50 , 300 , 400]
max_features = ['sqrt', 'log2']

# define grid search
grid = dict(n_estimators=n_estimators,max_features=max_features) # list of dicts
cv = RepeatedKfold(n_splits=10, n_repeats=3, random_state=1) #create CV
grid_search = GridSearchCV(estimator=model, param_grid=grid, n_jobs=-1, cv=cv,
scoring='neg_mean_absolute_error',error_score=0) #grid parameter
grid_result = grid_search.fit(X_train, y_train) #fit the grid

# summarize results
params = grid_result.best_params_
print("Best: %f" % grid_result.best_score_)
"""
means = grid_result.cv_results_['mean_test_score']
stds = grid_result.cv_results_['std_test_score']
params = grid_result.cv_results_['params']
for mean, stdev, param in zip(means, stds, params):
    print("%f (%f) with: %r" % (mean, stdev, param))
"""
means = grid_result.cv_results_['mean_test_score']

cnt = 0
print('model = RandomForestRegressor(' , end = ")
for key , value in params.items():
    cnt += 1
    if(type(value) == str):
        print(key, '=', '"" + value + "" , end = ")
    else:

```

```

    print(key , '=' , value , end = "")
    if cnt != len(params):
        print(end = ', ')
print("")
print("model.fit(X_train, y_train)")
print("y_pred = model.predict(X_test)")

model = RandomForestRegressor(max_features = 'log2', n_estimators = 400)
model.fit(X_train, y_train)
y_pred = model.predict(X_test)

scaled_result = model.predict(X_test)
unscaled_predict = scalerY.inverse_transform(scaled_result.reshape(-1 , 1))
unscaled_result = scalerY.inverse_transform(y_test.reshape(-1 , 1))
r2 = r2_score(unscaled_predict , unscaled_result)
rms = mean_squared_error(unscaled_predict , unscaled_result, squared=False)
print("r2: " , r2)
print("rms: " , rms)

```

The source code of Catboost algorithm is as follows.

```

# data analysis and wrangling
import pandas as pd
import numpy as np
import random as rnd

# visualization
import seaborn as sns
import matplotlib.pyplot as plt

```

```

from scipy.stats import norm
from scipy import stats
%matplotlib inline

# machine learning
from sklearn.linear_model import LinearRegression
from sklearn.ensemble import RandomForestRegressor
from sklearn.preprocessing import PolynomialFeatures
from sklearn.svm import SVR
from sklearn.ensemble import BaggingRegressor
from lightgbm import LGBMRegressor
from xgboost import XGBRegressor
from sklearn.ensemble import GradientBoostingRegressor
from sklearn.preprocessing import StandardScaler
from sklearn.metrics import mean_squared_error
from sklearn.metrics import r2_score
from catboost import CatBoostRegressor

#K-Cross-Validation
from sklearn.model_selection import RepeatedStratifiedKFold
from sklearn.model_selection import GridSearchCV
from sklearn.model_selection import RepeatedKFold
from sklearn.model_selection import KFold, cross_val_score, train_test_split

dataset = pd.read_excel('Data-for-ML.xlsx')
dataset["Sbet"].fillna(dataset["Sbet"].mean(), inplace = True)
dataset["%C"].fillna(dataset["%C"].mean(), inplace = True)

```

```

dataset["H/C"].fillna(dataset["H/C"].mean() , inplace = True)
dataset["(O+N)/C"].fillna(dataset["(O+N)/C"].mean() , inplace = True)
X = dataset.iloc[:, 1:-1].values
y = dataset.iloc[:, -1].values

scalerX = StandardScaler()
scaledX = scalerX.fit_transform(X)
X = scaledX
scalerY = StandardScaler()
scaledY = scalerY.fit_transform(y.reshape(-1 , 1))
y = scaledY.reshape(100)

from sklearn.model_selection import train_test_split
X_train, X_test, y_train, y_test = train_test_split(X, y, test_size = 0.15, random_state
= 1)

# define models and parameters

model = CatBoostRegressor()
parameters = {
    'depth'      : [6,8,10],
    'learning_rate' : [0.01, 0.05, 0.1],
    'iterations'  : [30, 50, 100]
}

# define grid search
grid = parameters # list of dicts
cv = RepeatedKfold(n_splits=10, n_repeats=3, random_state=1)
grid_search = GridSearchCV(estimator=model, param_grid=grid, n_jobs=-1, cv=cv,
scoring='neg_mean_absolute_error',error_score=0) # grid paramater

```

```

grid_result = grid_search.fit(X_train, y_train) # grid fit

# summarize results

params = grid_result.best_params_
print("Best: %f" % grid_result.best_score_)
"""

means = grid_result.cv_results_['mean_test_score']
stds = grid_result.cv_results_['std_test_score']
params = grid_result.cv_results_['params']
for mean, stdev, param in zip(means, stds, params):
    print("%f (%f) with: %r" % (mean, stdev, param))
"""

means = grid_result.cv_results_['mean_test_score']

cnt = 0
print('model = CatBoostRegressor(' , end = ")
for key , value in params.items():
    cnt += 1
    if(type(value) == str):
        print(key, '=', '"" + value + ""', end = ")
    else:
        print(key, '=', value , end = ")
    if cnt != len(params):
        print(end = ', ')
print(")")
print("model.fit(X_train, y_train)")
print("y_pred = model.predict(X_test)")

```

```

model = CatBoostRegressor(depth = 6, iterations = 100, learning_rate = 0.1)
model.fit(X_train, y_train)
y_pred = model.predict(X_test)

scaled_result = model.predict(X_test)
unscaled_predict = scalerY.inverse_transform(scaled_result.reshape(-1 , 1))
unscaled_result = scalerY.inverse_transform(y_test.reshape(-1 , 1))
r2 = r2_score(unscaled_predict , unscaled_result)
rms = mean_squared_error(unscaled_predict , unscaled_result, squared=False)
print("r2: " , r2)
print("rms: " , rms)

```

The source code of BRT algorithm is as follows.

```

# data analysis and wrangling
import pandas as pd
import numpy as np
import random as rnd

# visualization
import seaborn as sns
import matplotlib.pyplot as plt
from scipy.stats import norm
from scipy import stats

%matplotlib inline

# machine learning
from sklearn.linear_model import LinearRegression

```

```

from sklearn.ensemble import RandomForestRegressor
from sklearn.preprocessing import PolynomialFeatures
from sklearn.svm import SVR

from sklearn.ensemble import BaggingRegressor
from lightgbm import LGBMRegressor
from xgboost import XGBRegressor
from sklearn.ensemble import GradientBoostingRegressor
from sklearn.preprocessing import StandardScaler
from sklearn.metrics import mean_squared_error
from sklearn.metrics import r2_score

#K-Cross-Validation
from sklearn.model_selection import RepeatedStratifiedKFold
from sklearn.model_selection import GridSearchCV
from sklearn.model_selection import RepeatedKFold
from sklearn.model_selection import KFold, cross_val_score, train_test_split

dataset = pd.read_excel('/content/Data-for-ML.xlsx')
dataset["Sbet"].fillna(dataset["Sbet"].mean(), inplace = True)
dataset["%C"].fillna(dataset["%C"].mean(), inplace = True)
dataset["H/C"].fillna(dataset["H/C"].mean(), inplace = True)
dataset["(O+N)/C"].fillna(dataset["(O+N)/C"].mean(), inplace = True)

X = dataset.iloc[:, 1:-1].values
y = dataset.iloc[:, -1].values

scalerX = StandardScaler()
scaledX = scalerX.fit_transform(X)
X = scaledX
scalerY = StandardScaler()

```



```

scaledY = scalerY.fit_transform(y.reshape(-1 , 1))
y = scaledY.reshape(100)

from sklearn.model_selection import train_test_split
X_train, X_test, y_train, y_test = train_test_split(X, y, test_size = 0.15, random_state
= 1)

# define models and parameters
model = GradientBoostingRegressor()
n_estimators = [30 , 35 , 40 , 45 , 50]

# define grid search
grid = dict(n_estimators=n_estimators) # list of dicts
cv = RepeatedKfold(n_splits=10, n_repeats=3, random_state=1) #create CV
grid_search = GridSearchCV(estimator=model, param_grid=grid, n_jobs=-1, cv=cv,
scoring='neg_mean_absolute_error',error_score=0) #grid paramater
grid_result = grid_search.fit(X_train, y_train) #fit the grid

# summarize results
params = grid_result.best_params_
print("Best: %f" % grid_result.best_score_)
"""

means = grid_result.cv_results_['mean_test_score']
stds = grid_result.cv_results_['std_test_score']
params = grid_result.cv_results_['params']
for mean, stdev, param in zip(means, stds, params):
    print("%f (%f) with: %r" % (mean, stdev, param))
"""

means = grid_result.cv_results_['mean_test_score']

```

```

cnt = 0
print('model = GradientBoostingRegressor(' , end = ")
for key , value in params.items():
    cnt += 1
    if(type(value) == str):
        print(key, '=', "" + value + "" , end = ")
    else:
        print(key, '=', value , end = ")
    if cnt != len(params):
        print(end = ', ')
print(")")
print("model.fit(X_train, y_train)")
print("y_pred = model.predict(X_test)")

model = GradientBoostingRegressor(n_estimators = 50)
model.fit(X_train, y_train)
y_pred = model.predict(X_test)

scaled_result = model.predict(X_test)
unscaled_predict = scalerY.inverse_transform(scaled_result.reshape(-1 , 1))
unscaled_result = scalerY.inverse_transform(y_test.reshape(-1 , 1))
r2 = r2_score(unscaled_predict , unscaled_result)
rms = mean_squared_error(unscaled_predict , unscaled_result, squared=False)
print("r2: " , r2)
print("rms: " , rms)

```

REFERENCES

1. Gelband, H., et al., *The state of the world's antibiotics 2015*. Wound Healing Southern Africa, 2015. **8**(2): p. 30-34.
2. Chopra, I. and M. Roberts, *Tetracycline Antibiotics: Mode of Action, Applications, Molecular Biology, and Epidemiology of Bacterial Resistance*. Microbiology and Molecular Biology Reviews, 2001. **65**(2): p. 232-260.
3. Hu, X., Q. Zhou, and Y. Luo, *Occurrence and source analysis of typical veterinary antibiotics in manure, soil, vegetables and groundwater from organic vegetable bases, northern China*. Environ Pollut, 2010. **158**(9): p. 2992-8.
4. Krasucka, P., et al., *Engineered biochar – A sustainable solution for the removal of antibiotics from water*. Chemical Engineering Journal, 2021. **405**: p. 126926.
5. Yang, Y., et al., *Antibiotics and antibiotic resistance genes in global lakes: A review and meta-analysis*. Environment International, 2018. **116**: p. 60-73.
6. Organization, W.H. *Antibiotic resistance*. 2020; Available from: <https://www.who.int/news-room/fact-sheets/detail/antibiotic-resistance>.
7. Premarathna, K.S.D., et al., *Biochar-based engineered composites for sorptive decontamination of water: A review*. Chemical Engineering Journal, 2019. **372**: p. 536-550.
8. Shahbandeh, M. *Global production of fruit by variety selected 2020*. 2020 [cited 2022 January 26]; Available from: <https://www.statista.com/statistics/264001/worldwide-production-of-fruit-by-variety/>.
9. C. S. Chidan Kumar, R.M., S. Chandraju, *Studies on Sugars Extracted from Watermelon (Citrullus lanatus) Rind, A Remedy for Related Waste and Its Management*. International Journal of Chemical and Analytical Science, 2012. **3**(8): p. 1527-1529.
10. Reddy, N.A., R. Lakshmi pathy, and N.C. Sarada, *Application of Citrullus lanatus rind as biosorbent for removal of trivalent chromium from aqueous solution*. Alexandria Engineering Journal, 2014. **53**(4): p. 969-975.
11. Feumba Dibanda Romelle, A.R.P., and Ragu Sai Manohar, *CHEMICAL COMPOSITION OF SOME SELECTED FRUIT PEELS*. European Journal of Food Science and Technology, 2016. **4**: p. 12-21.
12. G. Gladvin, G.S., V. Swathi, and K. V. Santhisri, *Mineral and Vitamin Compositions Contents in Watermelon Peel (Rind)*. International Journal of Current Microbiology and Applied Sciences, 2017(5): p. 129-133.
13. Zhang, Y., et al., *Biomass Organs Control the Porosity of Their Pyrolyzed Carbon*. Advanced Functional Materials, 2017. **27**(3).
14. Dai, J., et al., *Effects of modification and magnetization of rice straw derived biochar on adsorption of tetracycline from water*. Bioresour Technol, 2020. **311**: p. 123455.
15. Liu, L., Y. Li, and S. Fan, *Preparation of KOH and H₃PO₄ Modified Biochar and Its Application in Methylene Blue Removal from Aqueous Solution*. Processes, 2019. **7**(12).
16. Li, X., et al., *Preparation and application of magnetic biochar in water treatment: A critical review*. Sci Total Environ, 2020. **711**: p. 134847.
17. Wang, S., et al., *Removal of arsenic by magnetic biochar prepared from*

- pinewood and natural hematite*. *Bioresour Technol*, 2015. **175**: p. 391-5.
18. Baig, S.A., et al., *Effect of synthesis methods on magnetic Kans grass biochar for enhanced As(III, V) adsorption from aqueous solutions*. *Biomass and Bioenergy*, 2014. **71**: p. 299-310.
 19. Yu, Z., X. Zhang, and Y. Huang, *Magnetic Chitosan–Iron(III) Hydrogel as a Fast and Reusable Adsorbent for Chromium(VI) Removal*. *Industrial & Engineering Chemistry Research*, 2013. **52**(34): p. 11956-11966.
 20. Zhang, P., et al., *A green biochar/iron oxide composite for methylene blue removal*. *Journal of Hazardous Materials*, 2020. **384**: p. 121286.
 21. Feng, Z., et al., *Preparation of magnetic biochar and its application in catalytic degradation of organic pollutants: A review*. *Sci Total Environ*, 2021. **765**: p. 142673.
 22. Bhattacharjee, C., S. Dutta, and V.K. Saxena, *A review on biosorptive removal of dyes and heavy metals from wastewater using watermelon rind as biosorbent*. *Environmental Advances*, 2020. **2**.
 23. Zhu, X., et al., *Machine learning for the selection of carbon-based materials for tetracycline and sulfamethoxazole adsorption*. *Chemical Engineering Journal*, 2021. **406**.
 24. Savic, I., et al., *Modelling and Optimization of Methylene Blue Adsorption from Aqueous Solution Using Bentonite Clay*, in *Computer Aided Chemical Engineering*, J.J. Klemesš, P.S. Varbanov, and P.Y. Liew, Editors. 2014, Elsevier. p. 1417-1422.
 25. Foroughi, M., et al., *Alum-based sludge (AbS) recycling for turbidity removal in drinking water treatment: an insight into statistical, technical, and health-related standpoints*. *Journal of Material Cycles and Waste Management*, 2018. **20**(4): p. 1999-2017.
 26. Zhu, X., et al., *Machine learning exploration of the critical factors for CO₂ adsorption capacity on porous carbon materials at different pressures*. *Journal of Cleaner Production*, 2020. **273**.
 27. O'NEILL, J., *ANTIMICROBIALS IN AGRICULTURE AND THE ENVIRONMENT: REDUCING UNNECESSARY USE AND WASTE*. 2015.
 28. Van Boeckel, T.P., et al., *Global trends in antimicrobial use in food animals*. *Proc Natl Acad Sci U S A*, 2015. **112**(18): p. 5649-54.
 29. Klein, E.Y., et al., *Global increase and geographic convergence in antibiotic consumption between 2000 and 2015*. *Proc Natl Acad Sci U S A*, 2018. **115**(15): p. E3463-E3470.
 30. Boleda, M.R., et al., *Survey of the occurrence of pharmaceuticals in Spanish finished drinking waters*. *Environmental Science and Pollution Research*, 2014. **21**(18): p. 10917-10939.
 31. Hu, X., Q. Zhou, and Y. Luo, *Occurrence and source analysis of typical veterinary antibiotics in manure, soil, vegetables and groundwater from organic vegetable bases, northern China*. *Environmental Pollution*, 2010. **158**(9): p. 2992-2998.
 32. Kwon, S.I., et al., *Applicability of the Charm II system for monitoring antibiotic residues in manure-based composts*. *Waste Management*, 2011. **31**(1): p. 39-44.
 33. Gothwal, R. and T. Shashidhar, *Antibiotic Pollution in the Environment: A Review*. *CLEAN – Soil, Air, Water*, 2015. **43**(4): p. 479-489.

34. Zhu, T.-t., et al., *Insights into the fate and removal of antibiotics and antibiotic resistance genes using biological wastewater treatment technology*. Science of The Total Environment, 2021. **776**: p. 145906.
35. Cuerda-Correa, E.M., M.F. Alexandre-Franco, and C. Fernández-González, *Advanced Oxidation Processes for the Removal of Antibiotics from Water. An Overview*. Water, 2020. **12**(1).
36. Liang, C., et al., *Removal of antibiotic resistance genes from swine wastewater by membrane filtration treatment*. Ecotoxicology and Environmental Safety, 2021. **210**: p. 111885.
37. Speed, D.E., *10 - Environmental aspects of planarization processes*, in *Advances in Chemical Mechanical Planarization (CMP)*, S. Babu, Editor. 2016, Woodhead Publishing. p. 229-269.
38. Artioli, Y., *Adsorption*, in *Encyclopedia of Ecology*, S.E. Jørgensen and B.D. Fath, Editors. 2008, Academic Press: Oxford. p. 60-65.
39. Shackley, S., et al., *Sustainable gasification–biochar systems? A case-study of rice-husk gasification in Cambodia, Part I: Context, chemical properties, environmental and health and safety issues*. Energy Policy, 2012. **42**: p. 49-58.
40. Sohi, S.P., et al., *Chapter 2 - A Review of Biochar and Its Use and Function in Soil*, in *Advances in Agronomy*. 2010, Academic Press. p. 47-82.
41. Ahmad, M., et al., *Biochar as a sorbent for contaminant management in soil and water: a review*. Chemosphere, 2014. **99**: p. 19-33.
42. Mohan, D., et al., *Organic and inorganic contaminants removal from water with biochar, a renewable, low cost and sustainable adsorbent – A critical review*. Bioresource Technology, 2014. **160**: p. 191-202.
43. Tan, X., et al., *Application of biochar for the removal of pollutants from aqueous solutions*. Chemosphere, 2015. **125**: p. 70-85.
44. Wang, B., B. Gao, and J. Fang, *Recent advances in engineered biochar productions and applications*. Critical Reviews in Environmental Science and Technology, 2017. **47**(22): p. 2158-2207.
45. Yang, X., et al., *Preparation and Modification of Biochar Materials and their Application in Soil Remediation*. Applied Sciences, 2019. **9**(7).
46. Sizmur, T., et al., *Biochar modification to enhance sorption of inorganics from water*. Bioresource Technology, 2017. **246**: p. 34-47.
47. Maschio G, K.C., Lucchesi A., *Pyrolysis, a promising route for biomass utilization*. Bioresour Technol, 1992. **42**: p. 219-31.
48. Yang, M.-T., et al., *Cobalt-impregnated biochar produced from CO₂-mediated pyrolysis of Co/lignin as an enhanced catalyst for activating peroxydisulfate to degrade acetaminophen*. Chemosphere, 2019. **226**: p. 924-933.
49. Zhao, L., et al., *Suppressed formation of polycyclic aromatic hydrocarbons (PAHs) during pyrolytic production of Fe-enriched composite biochar*. Journal of Hazardous Materials, 2020. **382**: p. 121033.
50. Thines, K.R., et al., *Synthesis of magnetic biochar from agricultural waste biomass to enhancing route for waste water and polymer application: A review*. Renewable and Sustainable Energy Reviews, 2017. **67**: p. 257-276.
51. Jolivet, J.P., C. Chanéac, and E. Tronc, *Iron oxide chemistry. From molecular clusters to extended solid networks*. Chem Commun (Camb), 2004(5): p. 481-7.
52. Myers, R.H., D.C. Montgomery, and C.M. Anderson-Cook, *Response surface*

- methodology: process and product optimization using designed experiments*. 2016: John Wiley & Sons.
53. Baş, D. and İ.H. Boyacı, *Modeling and optimization I: Usability of response surface methodology*. Journal of Food Engineering, 2007. **78**(3): p. 836-845.
 54. Khuri, A.I. and S. Mukhopadhyay, *Response surface methodology*. Wiley Interdisciplinary Reviews: Computational Statistics, 2010. **2**(2): p. 128-149.
 55. Nilsson, N.J., *The Quest for Artificial Intelligence: A History of Ideas and Achievements*. 2010, Cambridge University Press, New York, United States of America.
 56. Algren, M., W. Fisher, and A.E. Landis, *Chapter 8 - Machine learning in life cycle assessment*, in *Data Science Applied to Sustainability Analysis*, J. Dunn and P. Balaprakash, Editors. 2021, Elsevier. p. 167-190.
 57. Breiman, L., *RANDOM FORESTS*. 2001.
 58. Prokhorenkova, L., et al., *CatBoost: unbiased boosting with categorical features*. Advances in Neural Information Processing Systems 2018.
 59. Elith, J., J.R. Leathwick, and T. Hastie, *A working guide to boosted regression trees*. Journal of Animal Ecology, 2008. **77**(4): p. 802-813.
 60. Lingamdinne, L.P., et al., *Magnetic-watermelon rinds biochar for uranium-contaminated water treatment using an electromagnetic semi-batch column with removal mechanistic investigations*. Chemosphere, 2022. **286**: p. 131776.
 61. Hu, X., et al., *Effects of biomass pre-pyrolysis and pyrolysis temperature on magnetic biochar properties*. Journal of Analytical and Applied Pyrolysis, 2017. **127**: p. 196-202.
 62. Jiang, S.-F., et al., *High efficient removal of bisphenol A in a peroxymonosulfate/iron functionalized biochar system: Mechanistic elucidation and quantification of the contributors*. Chemical Engineering Journal, 2019. **359**: p. 572-583.
 63. Foroughi, M., M.H. Ahmadi Azqhandi, and S. Kakhki, *Bio-inspired, high, and fast adsorption of tetracycline from aqueous media using Fe₃O₄-g-CN@PEI-beta-CD nanocomposite: Modeling by response surface methodology (RSM), boosted regression tree (BRT), and general regression neural network (GRNN)*. J Hazard Mater, 2020. **388**: p. 121769.
 64. Topal, M. and E.I. Arslan Topal, *Optimization of tetracycline removal with chitosan obtained from mussel shells using RSM*. Journal of Industrial and Engineering Chemistry, 2020. **84**: p. 315-321.
 65. Nasiri, A., et al., *CoFe₂O₄@methylcellulose synthesized as a new magnetic nanocomposite to tetracycline adsorption: modeling, analysis, and optimization by response surface methodology*. Journal of Polymer Research, 2021. **28**(5).
 66. Kupgan, G., T.P. Liyana-Arachchi, and C.M. Colina, *NLDFT Pore Size Distribution in Amorphous Microporous Materials*. Langmuir, 2017. **33**(42): p. 11138-11145.
 67. Li, H., et al., *Effect of pyrolysis temperature on characteristics and aromatic contaminants adsorption behavior of magnetic biochar derived from pyrolysis oil distillation residue*. Bioresource Technology, 2017. **223**: p. 20-26.
 68. Selvarajoo, A. and D. Oochit, *Effect of pyrolysis temperature on product yields of palm fibre and its biochar characteristics*. Materials Science for Energy Technologies, 2020. **3**: p. 575-583.

69. Chatterjee, R., et al., *Effect of Pyrolysis Temperature on PhysicoChemical Properties and Acoustic-Based Amination of Biochar for Efficient CO₂ Adsorption*. *Frontiers in Energy Research*, 2020. **8**.
70. Chun, Y., et al., *Compositions and Sorptive Properties of Crop Residue-Derived Chars*. *Environmental Science & Technology*, 2004. **38**(17): p. 4649-4655.
71. Wang, H., et al., *Sorption of tetracycline on biochar derived from rice straw under different temperatures*. *PLoS One*, 2017. **12**(8): p. e0182776.
72. Fu, K., et al., *Activated carbon from tomato stem by chemical activation with FeCl₂*. *Colloids and Surfaces A: Physicochemical and Engineering Aspects*, 2017. **529**: p. 842-849.
73. Xu, Z., et al., *Insights into the pyrolysis behavior and adsorption properties of activated carbon from waste cotton textiles by FeCl₃-activation*. *Colloids and Surfaces A: Physicochemical and Engineering Aspects*, 2019. **582**: p. 123934.
74. Pimenta, M.A., et al., *Studying disorder in graphite-based systems by Raman spectroscopy*. *Phys Chem Chem Phys*, 2007. **9**(11): p. 1276-91.
75. Zhang, X., X. He, and S. Zhao, *Preparation of a novel Fe₃O₄@SiO₂@propyl@DBU magnetic core-shell nanocatalyst for Knoevenagel reaction in aqueous medium*. *Green Chemistry Letters and Reviews*, 2020. **14**(1): p. 85-98.
76. Hu Ping, K.L., Yang Jun, Yang Fan, Wang Kuaishe, Du Jinjing, Yang Zhanlin, Cao Weicheng, Liu Dongxin, *Synthesis of Fe Nanoparticles via One-Step Reduction Method*. *Rare Metal Materials and Engineering*, 2016. **45**(12): p. 3112-3114.
77. Bombuwala Dewage, N., et al., *Fast aniline and nitrobenzene remediation from water on magnetized and nonmagnetized Douglas fir biochar*. *Chemosphere*, 2019. **225**: p. 943-953.
78. Longbottom, R.J.a.K., Leiv. *Iron Ore Reduction with CO and H₂ Gas Mixtures – Thermodynamic and Kinetic Modelling*. 2008.
79. Marghussian, V., *4 - Magnetic Properties of Nano-Glass Ceramics*, in *Nano-Glass Ceramics*, V. Marghussian, Editor. 2015, William Andrew Publishing: Oxford. p. 181-223.
80. Willard, M., *Nanocrystalline Soft Magnetic Alloys: Two Decades of Progress*. 2013. p. 173-342.
81. Tripathi, M., et al., *Overview on Synthesis of Magnetic Bio Char from Discarded Agricultural Biomass*. 2016. p. 435.
82. Ho, Y.S. and G. McKay, *Pseudo-second order model for sorption processes*. *Process Biochemistry*, 1999. **34**(5): p. 451-465.
83. Panday, K.K., G. Prasad, and V.N. Singh, *Mixed adsorbents for Cu(II) removal from aqueous solutions*. *Environmental Technology Letters*, 1986. **7**(1-12): p. 547-554.
84. Ji, L., et al., *Mechanisms for strong adsorption of tetracycline to carbon nanotubes: A comparative study using activated carbon and graphite as adsorbents*. *Environmental Science & Technology*, 2009. **43**(7): p. 2322-2327.
85. Proctor, A. and J.F. Toro-Vazquez, *Chapter 10 - The Freundlich Isotherm in Studying Adsorption in Oil Processing*, in *Bleaching and Purifying Fats and Oils (Second Edition)*, G.R. List, Editor. 2009, AOCS Press. p. 209-219.
86. Zhao, Y., et al., *Interactions of tetracycline with Cd (II), Cu (II) and Pb (II) and*

- their cosorption behavior in soils*. Environ Pollut, 2013. **180**: p. 206-13.
87. Jang, H.M., et al., *Adsorption isotherm, kinetic modeling and mechanism of tetracycline on Pinus taeda-derived activated biochar*. Bioresour Technol, 2018. **259**: p. 24-31.
88. Mokhatab, S., W.A. Poe, and J.Y. Mak, *Chapter 9 - Natural Gas Dehydration and Mercaptans Removal*, in *Handbook of Natural Gas Transmission and Processing (Fourth Edition)*, S. Mokhatab, W.A. Poe, and J.Y. Mak, Editors. 2019, Gulf Professional Publishing. p. 307-348.
89. Abbar, B., et al., *Experimental investigation on removal of heavy metals (Cu 2+ , Pb 2+ , and Zn 2+) from aqueous solution by flax fibres*. Process Safety and Environmental Protection, 2017. **109**.
90. Ghadim, E.E., et al., *Adsorption properties of tetracycline onto graphene oxide: equilibrium, kinetic and thermodynamic studies*. PLoS One, 2013. **8**(11): p. e79254.





จุฬาลงกรณ์มหาวิทยาลัย
CHULALONGKORN UNIVERSITY

VITA

NAME	Phisit Thairattananon
DATE OF BIRTH	24 December 1997
PLACE OF BIRTH	Khon Kaen
INSTITUTIONS ATTENDED	M.Eng August 2020-Present Major: Chemical Engineering Chulalongkorn University, Bangkok, Thailand B.Eng August 2016 - May 2020 Major: Chemical Engineering Khon Kaen University, Khon Kaen, Thailand
PUBLICATION	Phisit Thairattananon, Giang T. T. Le, Noriaki Sano and Tawatchai Charinpanitkul, "Effect of pyrolysis temperature on magnetic biochar properties and adsorption capacity of tetracycline removal", Proceeding of the 10th Joint Conference on Renewable Energy and Nanotechnology (JCREN2021), Chiba, Japan, November 27th, 2021.